Adaptive overburden elimination with the multidimensional Marchenko equation

van der Neut, Joost; Wapenaar, Kees

DOI
10.1190/GEO2016-0024.1

Publication date
2016

Document Version
Final published version

Published in
Geophysics

GEOPHYSICS, VOL. 81, NO. 5 (SEPTEMBER-OCTOBER 2016); P. T265–T284, 21 FIGS., 1 TABLE.
10.1190/GEO2016-0024.1

Adaptive overburden elimination with the multidimensional Marchenko equation

Joost van der Neut[1] and Kees Wapenaar[1]

ABSTRACT

Iterative substitution of the multidimensional Marchenko equation has been introduced recently to integrate internal multiple reflections in the seismic imaging process. In so-called Marchenko imaging, a macro velocity model of the subsurface is required to meet this objective. The model is used to back-propagate the data during the first iteration and to truncate integrals in time during all successive iterations. In case of an erroneous model, the image will be blurred (akin to conventional imaging) and artifacts may arise from inaccurate integral truncations. However, the scheme is still successful in removing artifacts from internal multiple reflections. Inspired by these observations, we rewrote the Marchenko equation, such that it can be applied early in a processing flow, without the need of a macro velocity model. Instead, we have required an estimate of the two-way traveltime surface of a selected horizon in the subsurface. We have introduced an approximation, such that adaptive subtraction can be applied. As a solution, we obtained a new data set, in which all interactions (primaries and multiples) with the part of the medium above the picked horizon had been eliminated. Unlike various other internal multiple elimination algorithms, the method can be applied at any specified target horizon, without having to resolve for internal multiples from shallower horizons. We successfully applied the method on synthetic data, where limitations were reported due to thin layers, diffraction-like discontinuities, and a finite acquisition aperture. A field data test was also performed, in which the kinematics of the predicted updates were demonstrated to match with internal multiples in the recorded data, but it appeared difficult to subtract them.

INTRODUCTION

The occurrence of internal multiple reflections is a long-standing issue in seismic reflection imaging for marine acquisition (Hadidi and Verschuur, 1997; Van Borselen, 2002) and land acquisition (Alá'i and Verschuur, 2006; Kelamis et al., 2006; El-Emam et al., 2011). Various methods have been developed to predict and subtract internal multiples from recorded seismic data. In internal multiple elimination (IME), this is done in a layer-stripping fashion by back-propagating the recorded data to the various multiple generators in the subsurface and applying an algorithm based on multidimensional convolution and adaptive subtraction (Berkhout and Verschuur, 2005) or inversion (Ypma and Verschuur, 2013). As shown by Jakubowicz (1998), the back-propagation step can be replaced by a multidimensional crosscorrelation with primary reflections from the multiple generators. This approach requires identification of the internal multiple generators in the input data, but does not depend on a macro velocity model. The subtraction of the predicted internal multiples is typically applied with a least-squares matching filter, in which a minimum-energy criterion is imposed on the preserved primary reflections (Verschuur and Berkhout, 2005). Various case studies have demonstrated the success of this methodology to field data (Griffiths et al., 2011; King et al., 2013; Song et al., 2013; Cypriano et al., 2015).

Internal multiple reflections can also be estimated from the third (and higher order) term(s) in the inverse scattering series (ISS), derived from the Lippmann-Schwinger equation (Weglein et al., 1997) or from the Bremmer coupling series (Malcolm and de Hoop, 2004). Unlike in IME, all internal multiples are estimated at once, rather than through layer stripping. The ISS methodology can be interpreted as a migration-demigration process (Verschuur, 2013; Löer et al., 2016). Because any error in the macro model that is encountered during migration is compensated during demigration, the methodology appears to be relatively insensitive for errors in the macro model. However, computing the ISS requires accurate input

Manuscript received by the Editor 11 January 2016; revised manuscript received 19 May 2016; published online 25 August 2016.
[1]Delft University of Technology, Department of Geoscience and Engineering, Delft, The Netherlands. E-mail: j.r.vanderneut@tudelft.nl; c.p.a.wapenaar@tudelft.nl.

data with a relatively broad frequency band. Incomplete data, inaccurate source signature deconvolution, seismic attenuation, and other factors often require a matching filter to subtract the multiples predicted by the ISS from recorded field data, as shown by several studies (Matson et al., 1999; Luo et al., 2011; de Melo et al., 2014).

Recently, it was shown that internal multiple reflections can also be eliminated by solving the multidimensional Marchenko equation (Behura et al., 2014; Slob et al., 2014; Wapenaar et al., 2014b). With this approach, up- and downgoing Green's functions are retrieved at an arbitrary level in the subsurface. By multidimensional deconvolution of the retrieved upgoing Green's functions with the retrieved downgoing Green's functions at this level and evaluating the result at zero delay time (the imaging condition), an image emerges without artifacts from internal multiple reflections (Wapenaar et al., 2012; Broggini et al., 2014). The multidimensional deconvolution step can be expanded as a Neumann series and it can be shown that only the first term in this series contributes to the imaging condition (van der Neut et al., 2013). Because this first term is identical to the deconvolution of the retrieved upgoing Green's function with only the first event in the downgoing Green's function, an artifact-free image can also be constructed by crosscorrelation (or deconvolution) of these quantities, as demonstrated by van der Neut et al. (2015b).

Ravasi et al. (2016) apply the Marchenko equation to marine field data to image a local target zone either from above or below. Vasconcelos et al. (2015) demonstrate the effectiveness of the methodology in complex media and illustrate how prior knowledge of the medium's reflectivity can be integrated. Liu et al. (2016) use the Marchenko equation for local imaging below and above a borehole by combining seismic records at the surface with vertical seismic profile data. Although we restrict ourselves to solutions of the acoustic-wave equation in this paper, the Marchenko equation can also be derived for elastic media (da Costa Filho et al., 2014, 2015; Wapenaar and Slob, 2014). Consequently, the theory that is derived in this paper might also be extended to the elastic case.

Similar to the ISS and the method of Jakubowicz (1998), Marchenko imaging requires accurate reflection data. The source signature, source/receiver ghosts, and free-surface multiples should be removed from the initial recordings. Because seismic attenuation is not accounted for in the underlying theory (Wapenaar et al., 2014a) and the recorded data are generally incomplete (van der Neut et al., 2015a), amplitude mismatch is expected in the predicted internal multiples. To compensate for this mismatch, it can be beneficial to apply Marchenko imaging adaptively. Van der Neut et al. (2015b) describe a procedure for this, in which an adaptive procedure is applied at each image point. However, evaluation of the Marchenko equation at each image point individually tends to be expensive from a computational point of view.

As shown by Broggini et al. (2014), Marchenko imaging is not very sensitive to errors in the macro velocity model. To understand this observation, we should realize that, apart from blurring effects and imperfect integral truncations at high offsets, velocity errors manifest themselves mainly as time shifts in the retrieved Green's functions (similar to migration). By redatuming the retrieved Green's functions back to the acquisition surface through multidimensional convolution, we can undo this shift (similar to demigration), as illustrated by Meles et al. (2016). Hence, the combination of Marchenko redatuming and multidimensional convolution can be interpreted as a migration-demigration process, similar to other IME schemes. By predicting internal multiples at various depth levels in the subsurface and redatuming them to the acquisition level, an IME scheme can be derived (Meles et al., 2015). Alternatively, we can retrieve primary reflections at each depth level and redatum them to the acquisition level (Meles et al., 2016). This procedure requires processing multiple depth levels in a top-down approach, akin to various other IME schemes.

In this paper, we show how all interactions with the medium above a single horizon can be removed without first having to process shallower horizons. Moreover, we avoid the migration-demigration process that is embedded in the approach of Meles et al. (2015) by deriving an alternative Marchenko equation that can be evaluated directly at the acquisition level without a macro velocity model. Instead, we make use of a two-way traveltime surface of a single horizon that can be picked in the recorded data. The output of our scheme is a new data set that would be recorded if the medium above the selected horizon was nonreflective. These data can be migrated below the picked horizon, without suffering from any interaction with the overburden. We start with the derivation of an alternative Marchenko equation, which can be solved without a macro velocity model. Then, we show how the result can be used for IME by adaptive subtraction. The methodology is applied to a simple and a more complex synthetic data set and to marine field data. Finally, we discuss similarities and differences with existing IME methods. For the reader's convenience, we have provided a table with the various operators and wavefields that occur in Table 1.

Table 1. Overview of the operators and wavefields that occur in this paper.

Operator		Wavefield	
$\mathcal{R}$	Convolution with	G_d^+	Direct downgoing Green's function
	reflection response	U_d^+	Same, projected to acquisition surface
$\mathcal{R}^\star$	Crosscorrelation with	G_m^+	Coda of downgoing Green's function
	reflection response	U_m^+	Same, projected to acquisition surface
$\Theta_{t_x}^{t_y}$	Truncation of data	G^-	Upgoing Green's function
	outside $[t_x, t_y]$	U^-	Same, projected to acquisition surface
$\mathbf{\Omega}$	Combination of operators	f_{1d}^+	Direct downgoing focusing function
	$\Theta_{t_0}^{t_2}\mathcal{R}^\star\Theta_{t_0}^{t_2}\mathcal{R}$	δ	Same, projected to acquisition surface
$\mathbf{\Omega}^\star$	Combination of operators	f_{1m}^+	Coda of downgoing focusing function
	$\Theta_{-t_2}^{-t_0}\mathcal{R}\Theta_{-t_2}^{-t_0}\mathcal{R}^\star$	v_m^+	Same, projected to acquisition surface
$\mathcal{M}(\zeta)$	Convolution with ζ	f_1^-	Upgoing focusing function
	where $\zeta = U_m^+/U_d^+$	v_1^-	Same, projected to acquisition surface

CONVENTIONAL REPRESENTATIONS

In this paper, we indicate time as t and spatial locations as $\mathbf{x} = (\boldsymbol{\chi}, z)$, where $\boldsymbol{\chi}$ denotes the horizontal (x and y) coordinates and z denotes depth. An arbitrary wavefield is expressed as $P(\boldsymbol{\chi}_R, z_r; \boldsymbol{\chi}_S, z_s; t)$, where $\mathbf{x}_S = (\boldsymbol{\chi}_S, z_s)$ is the source location and $\mathbf{x}_R = (\boldsymbol{\chi}_R, z_r)$ is the receiver location. Note that we use lower case subscripts for z and upper case subscripts for $\mathbf{x}$ and $\boldsymbol{\chi}$. Consequently, we can easily define multiple source

and receiver locations at a specified depth level. We introduce the temporal Fourier transform

$$P(\boldsymbol{\chi}_R, z_r; \boldsymbol{\chi}_S, z_s; \omega) = \int_{-\infty}^{+\infty} dt e^{-j\omega t} P(\boldsymbol{\chi}_R, z_r; \boldsymbol{\chi}_S, z_s; t), \quad (1)$$

where j is the imaginary unit and ω is the angular frequency. In the derivations that follow, we will often switch between the time and frequency domain, depending on the nature of the problem. The seismic reflection response is expressed in the time domain as $R(\boldsymbol{\chi}_B, z_a; \boldsymbol{\chi}_A, z_a; t)$, where z_a denotes the acquisition depth level at which the data are recorded (i.e., the earth's surface). We emphasize that the reflection response does not contain a source signature. This means that the source signature should be deconvolved from the recorded data in practice. The sources and receivers are located at the acquisition surface Λ_a, being a transparent boundary at z_a. It is assumed that a nonreflective half-space exists above this level. In practice, this means that free-surface multiples should first be removed from the recorded data. However, the formulation can be extended to include free-surface multiples, as shown by Singh et al. (2015). Besides the reflection data, we make use of the so-called focusing function $f_1(\boldsymbol{\chi}_A, z_a; \boldsymbol{\chi}_F, z_f; t)$, being a particular solution of the source-free wave equation in a medium that is identical to the physical medium between the levels z_a and z_f, but which is reflection-free outside this domain. The focusing function is designed, such that it focuses at the focal point $\mathbf{x}_F = (\boldsymbol{\chi}_F, z_f)$, with $z_f > z_a$. We define Λ_f as a horizontal boundary of all potential focal $\boldsymbol{\chi}_F$ points at depth z_f. Finally, we define the Green's function $G(\boldsymbol{\chi}_F, z_f; \boldsymbol{\chi}_A, z_a; t)$ for the case that a source is excited at $\mathbf{x}_A$ and a receiver is positioned at the focal point $\mathbf{x}_F$. Unlike the focusing function, the Green's function is defined in the same medium as the recorded data. The focusing function and Green's function can be partitioned by separating their downgoing constituents (indicated by superscript $+$) G^+ and f_1^+, and their upgoing constituents (indicated by superscript $-$) G^- and f_1^-. Here, the upgoing and downgoing constituents are power-flux normalized (Wapenaar et al., 2014a). As a consequence of this normalization, these wavefields obey additional reciprocity relations, which will be exploited in this paper.

Most methodologies in seismic data processing can be interpreted by the actions of linear (e.g., migration, deghosting, etc.) operators on the recorded seismic data. In Marchenko redatuming, it seems more natural to interpret the recorded data as an operator, acting (multiple times) on (estimates of) the focusing function (van der Neut et al., 2015a). We adopt a similar philosophy in this paper. To simplify the notation, we introduce operator $\mathcal{R}$ for multidimensional convolution of an arbitrary wavefield $P(\boldsymbol{\chi}_B, z_a; \boldsymbol{\chi}_S, z_s; t)$ with the recorded reflection data, according to

$$\{\mathcal{R}P\}(\boldsymbol{\chi}_A, z_a; \boldsymbol{\chi}_S, z_s; t) = \int_{-\infty}^{+\infty} d\tau \int_{\Lambda_a} d^2\boldsymbol{\chi}_B R(\boldsymbol{\chi}_A, z_a; \boldsymbol{\chi}_B, z_a; \tau) P(\boldsymbol{\chi}_B, z_a; \boldsymbol{\chi}_S, z_s; t-\tau). \quad (2)$$

An equivalent operator $\mathcal{R}^\star$ is introduced for multidimensional crosscorrelation with the recorded reflection data:

$$\{\mathcal{R}^\star P\}(\boldsymbol{\chi}_A, z_a; \boldsymbol{\chi}_S, z_s; t) = \int_{-\infty}^{+\infty} d\tau \int_{\Lambda_a} d^2\boldsymbol{\chi}_B R(\boldsymbol{\chi}_A, z_a; \boldsymbol{\chi}_B, z_a; \tau) P(\boldsymbol{\chi}_B, z_a; \boldsymbol{\chi}_S, z_s; t+\tau). \quad (3)$$

Slob et al. (2014) and Wapenaar et al. (2014b) introduce two representations from which the multidimensional Marchenko equation can be derived. The first of these representations is of the convolution type and describes a multidimensional convolution of the downgoing part of the focusing function f_1^+ with the reflection data. We write this expression with the notation of equation 2 as

$$f_1^-(\boldsymbol{\chi}_A, z_a; \boldsymbol{\chi}_F, z_f; t) + G^-(\boldsymbol{\chi}_F, z_f; \boldsymbol{\chi}_A, z_a; t) = \{\mathcal{R}(f_{1d}^+ + f_{1m}^+)\}(\boldsymbol{\chi}_A, z_a; \boldsymbol{\chi}_F, z_f; t). \quad (4)$$

In this representation, we have separated the downgoing part of the focusing function into a direct part f_{1d}^+ and a coda f_{1m}^+. The direct part focuses the direct wavefield. It is essentially a classical redatuming operator that can be computed by inversion of the direct wavefield because it propagates in the physical medium. In practice, f_{1d}^+ is generally approximated by a time-reversed wavefield in a smooth macro velocity model (Broggini et al., 2014). If the medium was homogeneous between levels z_a and z_f, the coda f_{1m}^+ would vanish, as would f_1^- on the left side of equation 4. In this special case, equation 4 resembles a conventional redatuming scheme that ignores scattering in the overburden (Berryhill, 1984), where the upgoing Green's function G^- can be interpreted as redatumed data with a source at the acquisition level and a receiver at the focal point. However, when the medium is heterogeneous between z_a and z_f, a conventional redatuming scheme fails because reflections from the overburden will be mispositioned, leading to artifacts in the redatumed data space (Malcolm et al., 2007). Considering equation 4, these artifacts can be understood intuitively. Because f_{1m}^+ and f_1^- are nonzero in this case, f_{1d}^+ by itself is insufficient for reconstruction of the upgoing Green's function in this environment. The Marchenko equation as presented by Wapenaar et al. (2014a) can be interpreted as a tool to retrieve the missing components f_{1m}^+ and f_1^-, such that equation 4 can be used for retrieval of G^-, even below a heterogeneous overburden.

The second representation is of the correlation type and describes a multidimensional crosscorrelation of the upgoing part of the focusing function f_1^- with the reflection data. We write this representation with the help of equation 3 as

$$f_{1d}^+(\boldsymbol{\chi}_A, z_a; \boldsymbol{\chi}_F, z_f; t) + f_{1m}^+(\boldsymbol{\chi}_A, z_a; \boldsymbol{\chi}_F, z_f; t) - G_d^+(\boldsymbol{\chi}_F, z_f; \boldsymbol{\chi}_A, z_a; -t) - G_m^+(\boldsymbol{\chi}_F, z_f; \boldsymbol{\chi}_A, z_a; -t) = \{\mathcal{R}^\star f_1^-\}(\boldsymbol{\chi}_A, z_a; \boldsymbol{\chi}_F, z_f; t). \quad (5)$$

This result is only valid when the evanescent field is neglected. Horizontally propagating waves are not accounted for (Wapenaar et al., 2014b) and should be removed from the data. On the left side of equation 5, we find the downgoing focusing function $f_1^+(t)$ and the polarity- and time-reversed downgoing Green's function $-G^+(-t)$. Both these quantities are partitioned in a direct part (indicated by subscript d) and a coda (indicated by subscript m). In Marchenko redatuming, it is strictly assumed that $G_m^+(t)$ arrives later in time than $G_d^+(t)$. As a direct consequence of this assumption, $f_{1m}^+(t)$ arrives later in time than $f_{1d}^+(t)$ (Wapenaar et al., 2014a; van der Neut et al., 2015a). If the medium was homogeneous between z_a and z_f, the right side of equation 5 would vanish, as would $f_{1m}^+(t)$ and $G_m^+(-t)$ on the left side. In this special situation, we find that the time-reversed downgoing Green's function and the focusing function are identical.

In case of a heterogeneous overburden, however, this equality is no longer satisfied due to scattering losses in the overburden. Hence, the other terms in the equation should also be evaluated in this case.

The direct part of the downgoing focusing function can be interpreted as the inverse of the direct part of the downgoing Green's function. In the frequency domain, this can be expressed as (Wapenaar et al., 2014a)

$$\delta(\boldsymbol{\chi}_F' - \boldsymbol{\chi}_F) = \int_{\Lambda_a} d^2\boldsymbol{\chi}_B G_d^+(\boldsymbol{\chi}_F', z_f; \boldsymbol{\chi}_B, z_a; \omega) f_{1d}^+(\boldsymbol{\chi}_B, z_a; \boldsymbol{\chi}_F, z_f; \omega), \quad (6)$$

where $\delta(\boldsymbol{\chi}_F' - \boldsymbol{\chi}_F)$ is a spatially band-limited 2D delta function in space. We emphasize that equation 6 is only valid when the wavefields are power-flux normalized. By deriving an equivalent representation for the situation, where z_a and z_f are interchanged and applying source-receiver reciprocity, it follows that we may also write

$$\delta(\boldsymbol{\chi}_B' - \boldsymbol{\chi}_B) = \int_{\Lambda_f} d^2\boldsymbol{\chi}_F G_d^+(\boldsymbol{\chi}_F, z_f; \boldsymbol{\chi}_B', z_a; \omega) f_{1d}^+(\boldsymbol{\chi}_B, z_a; \boldsymbol{\chi}_F, z_f; \omega). \quad (7)$$

Note that in equation 7, the integral is carried out over Λ_f, whereas in equation 6, the integral is carried out over Λ_a. In this paper, we will use equation 7 extensively to collapse the direct part of the focusing function into a delta function at the acquisition surface.

REVISED REPRESENTATIONS

Wapenaar et al. (2014a) demonstrate how the multidimensional Marchenko equation can be derived from equations 4 and 5. The Marchenko equation could then be solved, given the reflection data R and an estimate of f_{1d}^+, which typically requires the use of a macro velocity model. In this paper, we take a different route by rewriting equations 4 and 5, such that they can be solved without knowledge of the direct focusing function. This is achieved by a multidimensional convolution of these representations with the direct wavefield $G_d^+(\boldsymbol{\chi}_F, z_f; \boldsymbol{\chi}_P, z_a; \omega)$, where $\mathbf{x}_P = (\boldsymbol{\chi}_P, z_a)$ is a projection point at the acquisition surface. For notational convenience, we define these projections in the frequency domain. We introduce the following definitions for the projected focusing functions:

$$v^-(\boldsymbol{\chi}_A, \boldsymbol{\chi}_P; \omega) = \int_{\Lambda_f} d^2\boldsymbol{\chi}_F G_d^+(\boldsymbol{\chi}_F, z_f; \boldsymbol{\chi}_P, z_a; \omega) f_1^-(\boldsymbol{\chi}_A, z_a; \boldsymbol{\chi}_F, z_f; \omega), \quad (8)$$

and

$$v_m^+(\boldsymbol{\chi}_A, \boldsymbol{\chi}_P; \omega) = \int_{\Lambda_f} d^2\boldsymbol{\chi}_F G_d^+(\boldsymbol{\chi}_F, z_f; \boldsymbol{\chi}_P, z_a; \omega) f_{1m}^+(\boldsymbol{\chi}_A, z_a; \boldsymbol{\chi}_F, z_f; \omega). \quad (9)$$

Because the projection point is always located at the acquisition surface throughout this paper, we omit to indicate depth z_a in the arguments of all projected wavefields, for notational convenience. We may refer to the quantities v^- and v_m^+ as virtual events, which is a terminology that was originally introduced by Ikelle (2006), who studies similar wavefields and demonstrates their use for IME. In a similar way as we did for the focusing function, we introduce the following projection of the upgoing Green's function:

$$U^-(\boldsymbol{\chi}_P, \boldsymbol{\chi}_A; \omega) = \int_{\Lambda_f} d^2\boldsymbol{\chi}_F G_d^+(\boldsymbol{\chi}_F, z_f; \boldsymbol{\chi}_P, z_a; \omega) G^-(\boldsymbol{\chi}_F, z_f; \boldsymbol{\chi}_A, z_a; \omega). \quad (10)$$

The wavefield U^- can be interpreted as a subset of the reflection data. This subset contains no data before the two-way traveltime of a fictitious reflector at horizon Λ_f. In Figure 1a, we illustrate that primaries are part of $U^-(t)$, whereas all multiples with a final (receiver side) reflection point above Λ_f (as illustrated in Figure 1b) are not part of this wavefield. Hence, particular internal multiples can be removed from the data by the retrieval of $U^-(t)$. In Figure 1c and 1d, we also show internal multiples with their final (receiver side) reflection point below Λ_f. Because these multiples are part of $U^-(t)$, they need to be removed by an additional processing step, as we will show later in the paper. If we convolve equation 4 with $G_d^+(\boldsymbol{\chi}_F, z_f; \boldsymbol{\chi}_P, z_a; \omega)$ and integrate over $\boldsymbol{\chi}_F$, we find with the help of equations 7–10:

$$v^-(\boldsymbol{\chi}_A, \boldsymbol{\chi}_P; t) + U^-(\boldsymbol{\chi}_P, \boldsymbol{\chi}_A; t) = \{\mathcal{R}(\delta + v_m^+)\}(\boldsymbol{\chi}_A, \boldsymbol{\chi}_P; t). \quad (11)$$

In this expression, we defined

$$\{\mathcal{R}\delta\}(\boldsymbol{\chi}_A, \boldsymbol{\chi}_P; t) = R(\boldsymbol{\chi}_A, \boldsymbol{\chi}_P; t), \quad (12)$$

being the data as recorded at the acquisition surface. Due to the projection, the direct part of the focusing function has collapsed to a delta function. A similar projection can be applied in equation 5. Because the downgoing Green's function is time reversed in this expression, this wavefield will be crosscorrelated (rather than convolved) by this projection. Therefore, we define the following quantities in the frequency domain:

$$U_d^+(\boldsymbol{\chi}_P, \boldsymbol{\chi}_A; \omega) = \int_{\Lambda_f} d^2\boldsymbol{\chi}_F G_d^{+*}(\boldsymbol{\chi}_F, z_f; \boldsymbol{\chi}_P, z_a; \omega) G_d^+(\boldsymbol{\chi}_F, z_f; \boldsymbol{\chi}_A, z_a; \omega), \quad (13)$$

and

$$U_m^+(\boldsymbol{\chi}_P, \boldsymbol{\chi}_A; \omega) = \int_{\Lambda_f} d^2\boldsymbol{\chi}_F G_d^{+*}(\boldsymbol{\chi}_F, z_f; \boldsymbol{\chi}_P, z_a; \omega) G_m^+(\boldsymbol{\chi}_F, z_f; \boldsymbol{\chi}_A, z_a; \omega). \quad (14)$$

Now, if we convolve equation 5 (after Fourier transformation) with $G_d^+(\boldsymbol{\chi}_F, z_f; \boldsymbol{\chi}_P, z_a; \omega)$ and integrate over $\boldsymbol{\chi}_F$, it follows (after inverse Fourier transformation) that

$$\delta(\boldsymbol{\chi}_P - \boldsymbol{\chi}_A)\delta(t) + v_m^+(\boldsymbol{\chi}_A, \boldsymbol{\chi}_P; t) - U_d^+(\boldsymbol{\chi}_P, \boldsymbol{\chi}_A; -t) - U_m^+(\boldsymbol{\chi}_P, \boldsymbol{\chi}_A; -t) = \{\mathcal{R}^\star v^-\}(\boldsymbol{\chi}_A, \boldsymbol{\chi}_P; t), \quad (15)$$

where we made use of equations 7–9, 13, and 14. Once again, the direct part of the focusing function has collapsed to a delta function. In the next section, we will derive a Marchenko equation from

expressions 11 and 15, which can be solved for the functions v^- and v_m^+, without knowledge of the initial focusing function.

MARCHENKO EQUATION

When deriving the Marchenko equation, we should account for the final bandwidth of the data. For this purpose, we introduce a zero-phase wavelet $W(t)$ with finite support $[-t_w, t_w]$ that imposes band limitation. This wavelet can be chosen arbitrarily within the bandwidth of the recorded data. We convolve equations 11 and 15 with this wavelet, leading to

$$\widehat{v^-}(\boldsymbol{\chi}_A,\boldsymbol{\chi}_P;t)+\widehat{U^-}(\boldsymbol{\chi}_P,\boldsymbol{\chi}_A;t)=\{\mathcal{R}(\widehat{\delta}+\widehat{v_m^+})\}(\boldsymbol{\chi}_A,\boldsymbol{\chi}_P;t), \quad (16)$$

and

$$\begin{aligned}&\delta(\boldsymbol{\chi}_P-\boldsymbol{\chi}_A)\widehat{\delta}(t)+\widehat{v_m^+}(\boldsymbol{\chi}_A,\boldsymbol{\chi}_P;t)\\&\quad-\widehat{U_d^+}(\boldsymbol{\chi}_P,\boldsymbol{\chi}_A;-t)-\widehat{U_m^+}(\boldsymbol{\chi}_P,\boldsymbol{\chi}_A;-t)\\&\quad=\{\mathcal{R}^\star\widehat{v^-}\}(\boldsymbol{\chi}_A,\boldsymbol{\chi}_P;t).\end{aligned} \quad (17)$$

In these equations, the $\widehat{\ }$ symbol denotes that a wavefield has been convolved with $W(t)$. We will now show how a Marchenko equation can be derived from these results. To do so, we apply time windowing through operators of the form $\Theta_{t_x}^{t_y}$, where $t_x \le t_y$. The action of such an operator on an arbitrary wavefield $P(\boldsymbol{\chi}_A,\boldsymbol{\chi}_B;t)$ is defined as

$$\begin{aligned}\{\Theta_{t_x}^{t_y}P\}(\boldsymbol{\chi}_A,\boldsymbol{\chi}_B;t)&=(\theta(t-t_x)\\&\quad-\theta(t-t_y))P(\boldsymbol{\chi}_A,\boldsymbol{\chi}_B;t).\end{aligned} \quad (18)$$

In this expression, $\theta(t)$ is a Heaviside function (where $\theta(t)=0$ for $t<0$, $\theta(t)=(1/2)$ for $t=0$, and $\theta(t)=1$ for $t>0$). Note that operator $\Theta_{t_x}^{t_y}$ preserves the signal in the domain $[t_x,t_y]$, but removes all samples outside this domain. The truncation times $t_x(\boldsymbol{\chi}_A,\boldsymbol{\chi}_B)$ and $t_y(\boldsymbol{\chi}_A,\boldsymbol{\chi}_B)$ are defined as functions of source and receiver coordinates, which we have omitted for notational convenience.

In the conventional Marchenko equation, truncations are applied to equations 4 and 5, using a one-way traveltime surface of the direct wave $t_1(\boldsymbol{\chi}_A,\boldsymbol{\chi}_F)$, which can be computed from a macro velocity model. In practice, $t_1(\boldsymbol{\chi}_A,\boldsymbol{\chi}_F)$ is chosen t_w (half the support of the wavelet) before the direct wavelet to account for the finite-frequency content of the data. We make use of the fact that the Green's functions and focusing functions reside in different sections of the time domain (van der Neut et al., 2015a), as indicated in Figure 2a. As shown in Figure 2b, the wavefields that occur in equations 16 and 17 are also separated in time. Because all wavefields have been redatumed with the direct wavefield, truncations should now be applied at two-way traveltimes, rather than at the one-way traveltimes. We define $t_2(\boldsymbol{\chi}_A,\boldsymbol{\chi}_P)$ as a two-way traveltime surface of a potential reflector at horizon Λ_f, which can be picked in the recorded data. The part of the medium above this horizon can be interpreted as the overburden. Our objective is to remove all interactions with this overburden from the recorded data. Note that Λ_f does not necessarily need to be horizontal. A more important criterion is that any upgoing wave at this horizon should arrive at least t_w after the direct downgoing wave, being a fundamental assumption to derive the Marchenko equation. In case of thin layers, this assumption is not always fulfilled, posing limitations to the methodology, as pointed out by Slob et al. (2014). In the examples, we will show that the method still works well in case boundary Λ_f is moderately dipping. The exact limitations for nonhorizontal Λ_f will not be investigated in this paper, but they are assumed to be similar to other IME schemes that use pseudoboundaries in the subsurface, such as those of Jakubowicz (1998), Van Borselen (2002), Verschuur and Berkhout (2005), Griffiths et al. (2011), and many others. Intersections of Λ_f with medium discontinuities can result

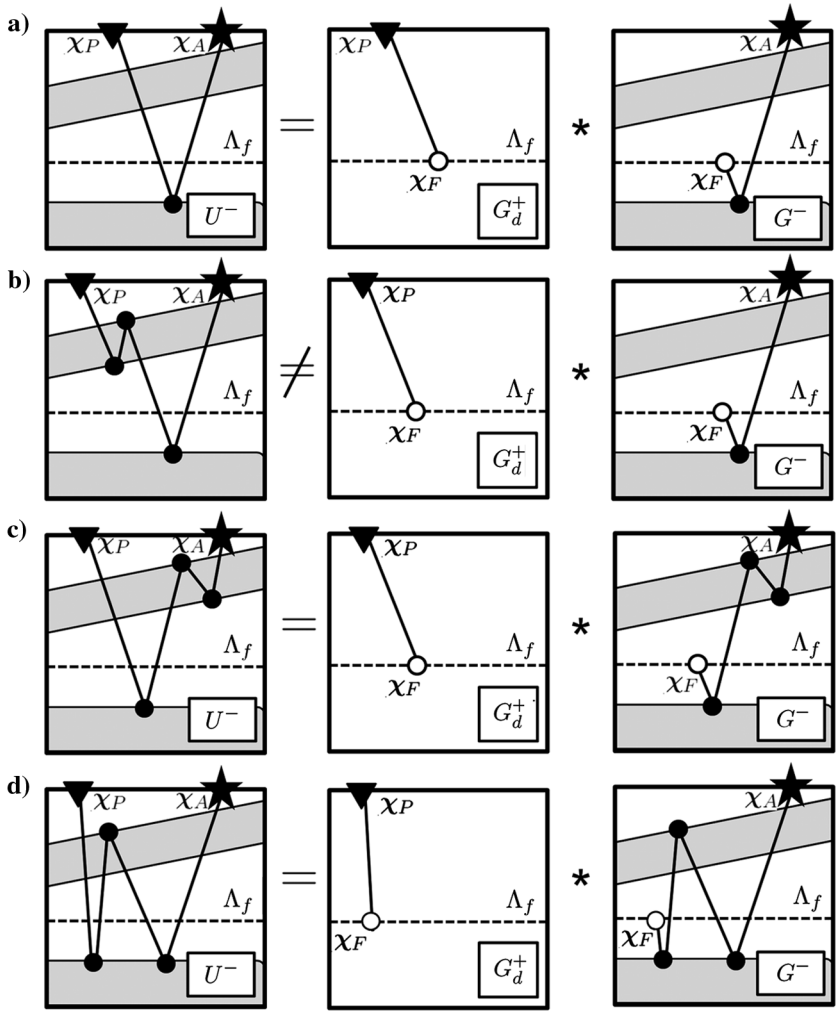

Figure 1. Illustration of equation 10. (a) Primaries that have passed horizon Λ_f are constructed by multidimensional convolution of $G_d^+(\boldsymbol{\chi}_F,z_f;\boldsymbol{\chi}_P,z_a;t)$ and $G^-(\boldsymbol{\chi}_F,z_f;\boldsymbol{\chi}_A,z_a;t)$. (b) Internal multiples with the last (receiver side) reflection point above Λ_f are not constructed with equation 10. Hence, these multiples are not part of $U^-(\boldsymbol{\chi}_P,\boldsymbol{\chi}_A;t)$. (c and d) Internal multiples with the last (receiver side) reflection point below Λ_f are being constructed in equation 10. Hence, these multiples are part of $U^-(\boldsymbol{\chi}_P,\boldsymbol{\chi}_A;t)$.

in artifacts and are to be avoided. For an illustration of such artifacts, see Meles et al. (2016).

Further, we define a traveltime surface $t_0(\boldsymbol{\chi}_A,\boldsymbol{\chi}_P)$ to differentiate between direct wave propagation and internal multiple reflections. This traveltime surface should separate the wavefields $\widehat{U}_d^+(t)$ and $\widehat{\delta}(t)$ from $\widehat{U}_m^+(t)$ and $\widehat{v}_m^+(t)$. As shown in Figure 2b, t_0 should be picked just after $t=0$ to meet this objective. Because of the finite-frequency content of the data, such separation can only be established if the internal multiples are sufficiently delayed in terms of traveltime. As in conventional Marchenko redatuming, the resolution is limited by $t_0(\boldsymbol{\chi}_P,\boldsymbol{\chi}_P)=t_w$ at zero offset, being half the support of the wavelet. In the numerical examples, we show how $t_0(\boldsymbol{\chi}_A,\boldsymbol{\chi}_P)$ can be estimated at nonzero offsets.

Given the traveltime surfaces $t_0(\boldsymbol{\chi}_A,\boldsymbol{\chi}_P)$ and $t_2(\boldsymbol{\chi}_A,\boldsymbol{\chi}_P)$, we can construct a window operator $\Theta_{t_0}^{t_2}$, which effectively removes all data later than t_2, the redatumed direct wavefield (arriving just before t_0) and all acausal components. Because $\widehat{U}^-(t)$ contains no information before t_2, it follows that $\{\Theta_{t_0}^{t_2}\widehat{U}^-\}(t)=0$. Further because $\widehat{v}^-(t)$ contains no data outside the interval $[t_0,t_2]$, we find $\{\Theta_{t_0}^{t_2}\widehat{v}^-\}(t)=\widehat{v}^-(t)$. Consequently, applying the operator $\Theta_{t_0}^{t_2}$ to equation 16 yields

$$\widehat{v}^-(\boldsymbol{\chi}_P,\boldsymbol{\chi}_A;t)=\{\Theta_{t_0}^{t_2}\mathcal{R}(\widehat{\delta}+\widehat{v}_m^+)\}(\boldsymbol{\chi}_A,\boldsymbol{\chi}_P;t). \tag{19}$$

Based on a similar reasoning, it follows that $\{\Theta_{t_0}^{t_2}\widehat{v}_m^+\}(t)=\widehat{v}_m^+(t)$, $\{\Theta_{t_0}^{t_2}\widehat{\delta}\}(t)=0$, $\{\Theta_{t_0}^{t_2}\widehat{U}_m^+\}(-t)=0$, and $\{\Theta_{t_0}^{t_2}\widehat{U}_d^+\}(-t)=0$. Hence, the action of $\Theta_{t_0}^{t_2}$ on equation 17 yields

$$\widehat{v}_m^+(\boldsymbol{\chi}_A,\boldsymbol{\chi}_P;t)=\{\Theta_{t_0}^{t_2}\mathcal{R}^\star\widehat{v}^-\}(\boldsymbol{\chi}_A,\boldsymbol{\chi}_P;t). \tag{20}$$

Equations 19 and 20 can be combined to derive a revised Marchenko equation. This is done by substitution of equation 19 into equation 20, yielding

$$\{\Omega\widehat{\delta}\}(\boldsymbol{\chi}_A,\boldsymbol{\chi}_P;t)=\widehat{v}_m^+(\boldsymbol{\chi}_A,\boldsymbol{\chi}_P;t)-\{\Omega\widehat{v}_m^+\}(\boldsymbol{\chi}_A,\boldsymbol{\chi}_P;t), \tag{21}$$

with the kernel

$$\Omega=\Theta_{t_0}^{t_2}\mathcal{R}^\star\Theta_{t_0}^{t_2}\mathcal{R}. \tag{22}$$

Similar to the Marchenko equation of Wapenaar et al. (2014a), equation 21 is a Fredholm integral equation of the second kind, which can be expanded as a Neumann series. This yields the solution

$$\widehat{v}_m^+(\boldsymbol{\chi}_A,\boldsymbol{\chi}_P;t)=\sum_{k=1}^{\infty}\{\Omega^k\widehat{\delta}\}(\boldsymbol{\chi}_A,\boldsymbol{\chi}_P;t). \tag{23}$$

Here, Ω^k means that operator Ω is applied k times. As shown by Fokkema and van den Berg (1993), convergence of this series is guaranteed if $|\{\Omega^k\delta\}(\boldsymbol{\chi}_A,\boldsymbol{\chi}_P;t)|_2\to 0$ as $k\to\infty$, where subscript 2 denotes the ℓ_2-norm. This condition is satisfied when the norms of operators $\mathcal{R}$ and $\mathcal{R}^\star$ are less than one, meaning that $|\mathcal{R}P|_2\le|P|_2$ and $|\mathcal{R}^\star P|_2\le|P|_2$ for any wavefield P. An equivalent solution for $\widehat{v}^-$ can be found by substituting equation 23 into equation 19, leading to

$$\widehat{v}^-(\boldsymbol{\chi}_P,\boldsymbol{\chi}_A;t)=\sum_{k=0}^{\infty}\{\Theta_{t_0}^{t_2}\mathcal{R}\Omega^k\widehat{\delta}\}(\boldsymbol{\chi}_P,\boldsymbol{\chi}_A;t). \tag{24}$$

This result is almost similar to the solution of the multidimensional Marchenko equation of Wapenaar et al. (2014a), which can also be written as a series (van der Neut et al., 2015a). However, because the focusing functions are projected to the acquisition surface, the initial focusing function is replaced by a spatial and temporal delta function $\delta(\boldsymbol{\chi}_P-\boldsymbol{\chi}_A)\widehat{\delta}(t)$, which is independent of a macro velocity model. As a consequence, the signals should not be truncated at one-way traveltimes, as in the solution of the original Marchenko equation, but at t_0 (just after the redatumed direct wavefield that maps at $t=0$) and at the two-way traveltime t_2 of a fictitious reflector at horizon Λ_f.

To retrieve the projected wavefield $\widehat{U}^-(t)$, equation 23 can be substituted into equation 16. After applying the window operator $\Theta_{t_2}^{\infty}$ to the result and using the relations $\{\Theta_{t_2}^{\infty}\widehat{v}^-\}(t)=0$ and $\{\Theta_{t_2}^{\infty}\widehat{U}^-\}(t)=\widehat{U}^-(t)$, we find

$$\widehat{U}^-(\boldsymbol{\chi}_P,\boldsymbol{\chi}_A;t)=\sum_{k=0}^{\infty}\{\Theta_{t_2}^{\infty}\mathcal{R}\Omega^k\widehat{\delta}\}(\boldsymbol{\chi}_P,\boldsymbol{\chi}_A;t). \tag{25}$$

The first term in this series can be interpreted as the truncated data. The remaining terms describe the internal multiples that should be subtracted from the truncated data to preserve only the events that obey equation 10. As we explained earlier in the paper, $\widehat{U}^-(t)$ can be interpreted as reflection data, where particular multiples, as indicated in Figure 1b, have been eliminated. However, the multiples that are indicated in Figure 1c and 1d are still part of $U^-(t)$ and should be eliminated by another processing step. This step will be derived in the following section.

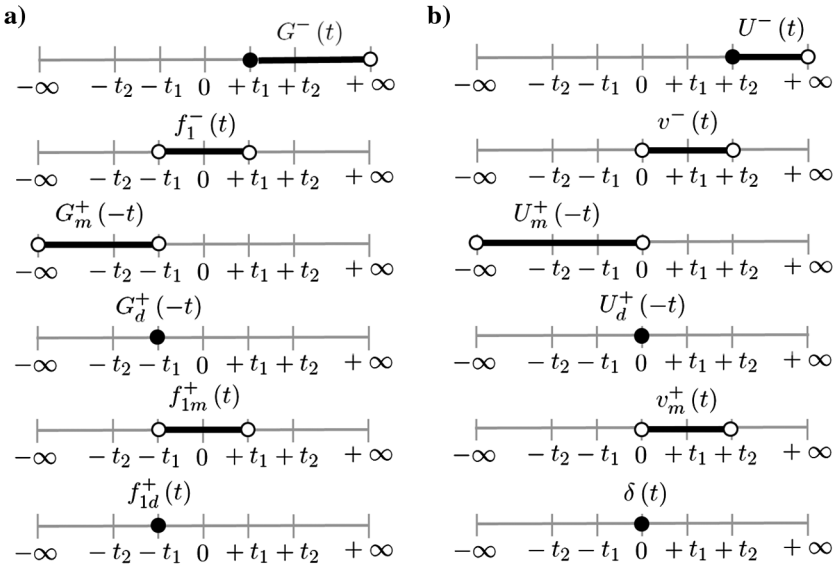

Figure 2. The wavefields that are discussed in this paper reside in different sections of the time domain. (a) The wavefields in equations 4 and 5 separate at the one-way traveltime of the direct wave t_1 (van der Neut et al., 2015a). (b) Wavefields in the revised equations 16 and 17 separate at t_0, which is chosen just after $t=0$ to account for the finite-frequency content of the data and at t_2, which is the two-way traveltime of the overburden.

The projected downgoing Green's functions $\widehat{U}_d^+(t)$ and $\widehat{U}_m^+(t)$ can be constructed by a similar procedure. For the retrieval of $\widehat{U}_d^+(t)$, we introduce window operator $\Theta_{-t_0}^{+t_0}$, which removes all but the redatumed direct wavefield, mapping at the origin of the gathers (i.e., at $t=0$ and $\boldsymbol{\chi}_A=\boldsymbol{\chi}_P$). We will use the observations that $\{\Theta_{-t_0}^{+t_0}\widehat{v}_m^+\}(-t)=0$, $\{\Theta_{-t_0}^{+t_0}\widehat{U}_m^+\}(t)=0$, $\{\Theta_{-t_0}^{+t_0}\widehat{U}_d^+\}(t)=\widehat{U}_d^+(t)$, and $\{\Theta_{-t_0}^{+t_0}\widehat{\delta}\}(t)=\widehat{\delta}(t)$. Based on these conditions, it now follows from the action of $\Theta_{-t_0}^{+t_0}$ on equation 17 (after substituting equation 24 and time reversing all wavefields and operators) that

$$\widehat{U}_d^+(\boldsymbol{\chi}_P,\boldsymbol{\chi}_A;t)=\widehat{\delta}(\boldsymbol{\chi}_P-\boldsymbol{\chi}_A)\widehat{\delta}(t)-\sum_{k=0}^{\infty}\{\Theta_{-t_0}^{+t_0}\mathcal{R}\Theta_{-t_2}^{-t_0}\mathcal{R}^\star\Omega^{\star k}\widehat{\delta}\}(\boldsymbol{\chi}_P,\boldsymbol{\chi}_A;t). \quad (26)$$

Here, we have defined additionally

$$\Omega^\star=\Theta_{-t_2}^{-t_0}\mathcal{R}\Theta_{-t_2}^{-t_0}\mathcal{R}^\star. \quad (27)$$

Equation 26 can be useful to estimate the scattering transmission losses in the medium. Remember that $\widehat{U}_d^+(t)$ can be interpreted as the autocorrelation of the downgoing wavefield at horizon Λ_f in the actual medium (see equation 13). It is interesting to observe that this measure can be computed without a macro velocity model. The only requirements are a two-way traveltime curve that allows us to define the truncation time for the window operator and the recorded reflection data to construct operators $\mathcal{R}$ and $\mathcal{R}^\star$.

Instead of $\widehat{U}_d^+(t)$, we can also choose to isolate $\widehat{U}_m^+(t)$ in the left side of equation 17 (after time reversing all wavefields and operators). This is done by applying the window operator $\Theta_{t_0}^{\infty}$, removing all information before t_0. By realizing that $\{\Theta_{t_0}^{\infty}\widehat{v}_m^+\}(-t)=0$, $\{\Theta_{t_0}^{\infty}\widehat{U}_d^+\}(t)=0$, $\{\Theta_{t_0}^{\infty}\widehat{\delta}\}(t)=0$, and $\{\Theta_{t_0}^{\infty}\widehat{U}_m^+\}(t)=\widehat{U}_m^+(t)$, we find (after substituting equation 24)

$$\widehat{U}_m^+(\boldsymbol{\chi}_P,\boldsymbol{\chi}_A;t)=-\sum_{k=0}^{\infty}\{\Theta_{t_0}^{\infty}\mathcal{R}\Theta_{-t_2}^{-t_0}\mathcal{R}^\star\Omega^{\star k}\widehat{\delta}\}(\boldsymbol{\chi}_P,\boldsymbol{\chi}_A;t). \quad (28)$$

We will see in the next section how this result can be used to remove the remaining internal multiples from $\widehat{U}^-(t)$.

INTERNAL MULTIPLE ELIMINATION

As we mentioned before, the wavefield $\widehat{U}^-(t)$ as computed in equation 25 can be interpreted as a subset of the recorded data that has reflected at least once below Λ_f, where internal multiples "at the receiver side" (such as those that are indicated by Figure 1b) have been removed. At this point, however, the IME process is incomplete because other undesired interactions with the overburden are still preserved in $\widehat{U}^-(t)$, as indicated by Figure 1c and 1d. In the remainder of this paper, we will show how the events that are encoded in the projected downgoing wavefield $\widehat{U}_m^+(t)$ (as computed in equation 28) can be used to remove all remaining internal multiples from the projected upgoing wavefield $\widehat{U}^-(t)$, leading to a new data set, which does not contain primary and multiple reflections from the overburden.

We start with a forward model from Wapenaar et al. (2011), where the upgoing wavefield $\widehat{G}^-$ at level Λ_f is related to the downgoing wavefield $\widehat{G}^+$ at the same level, through the following integral representation (expressed in the frequency domain):

$$\widehat{G}^-(\boldsymbol{\chi}_F,z_f;\boldsymbol{\chi}_A,z_a;\omega)=\int_{\Lambda_f}d^2\boldsymbol{\chi}_G X_f(\boldsymbol{\chi}_F,z_f;\boldsymbol{\chi}_G,z_f;\omega)(\widehat{G}_d^+(\boldsymbol{\chi}_G,z_f;\boldsymbol{\chi}_A,z_a;\omega)+\widehat{G}_m^+(\boldsymbol{\chi}_G,z_f;\boldsymbol{\chi}_A,z_a;\omega)). \quad (29)$$

Once again, we separated the downgoing wavefield into a direct part G_d^+ and a coda G_m^+. Further, $X_f(\boldsymbol{\chi}_F,z_f;\boldsymbol{\chi}_G,z_f;\omega)$ is a reflection response at $\mathbf{x}_F$ due to a source at $\mathbf{x}_G$. Both these locations are at horizon Λ_f and special boundary conditions are applied, such that the medium is nonreflective above this horizon (which is indicated by subscript f). Hence, $X_f(t)$ contains no (first- and higher-order) interactions with the medium above Λ_f.

Equation 29 can be redatumed to the acquisition surface. To do so, we realize that the direct part of the downgoing Green's function can be expressed as

$$\widehat{G}_d^+(\boldsymbol{\chi}_G,z_f;\boldsymbol{\chi}_A,z_a;\omega)=\int_{\Lambda_a}d^2\boldsymbol{\chi}_Q\widehat{G}_d^+(\boldsymbol{\chi}_G,z_f;\boldsymbol{\chi}_Q,z_a;\omega)\delta(\boldsymbol{\chi}_Q-\boldsymbol{\chi}_A). \quad (30)$$

For the coda of the downgoing Green's function, we assume the existence of a function ζ, such that

$$\widehat{G}_m^+(\boldsymbol{\chi}_G,z_f;\boldsymbol{\chi}_A,z_a;\omega)=\int_{\Lambda_a}d^2\boldsymbol{\chi}_Q\widehat{G}_d^+(\boldsymbol{\chi}_G,z_f;\boldsymbol{\chi}_Q,z_a;\omega)\zeta(\boldsymbol{\chi}_Q,\boldsymbol{\chi}_A;\omega). \quad (31)$$

When we substitute equations 30 and 31 into equation 29 and we convolve both sides with $G_d^+(\boldsymbol{\chi}_F,z_f;\boldsymbol{\chi}_P,z_a;\omega)$ (where integration is carried out over $\boldsymbol{\chi}_F$), it follows that with the help of equation 10, after changing the order of the integrals that

$$\widehat{U}^-(\boldsymbol{\chi}_P,\boldsymbol{\chi}_A;\omega)=\int_{\Lambda_a}d^2\boldsymbol{\chi}_Q\widehat{R}_f(\boldsymbol{\chi}_P;\boldsymbol{\chi}_Q;\omega)(\delta(\boldsymbol{\chi}_Q-\boldsymbol{\chi}_A)+\zeta(\boldsymbol{\chi}_Q,\boldsymbol{\chi}_A;\omega)), \quad (32)$$

where we introduced

$$\widehat{R}_f(\boldsymbol{\chi}_P,\boldsymbol{\chi}_Q;\omega)=\int_{\Lambda_f}d^2\boldsymbol{\chi}_F\int_{\Lambda_f}d^2\boldsymbol{\chi}_G G_d^+(\boldsymbol{\chi}_F,z_f;\boldsymbol{\chi}_P,z_a;\omega)X_f\times(\boldsymbol{\chi}_F,z_f;\boldsymbol{\chi}_G,z_f;\omega)\widehat{G}_d^+(\boldsymbol{\chi}_G,z_f;\boldsymbol{\chi}_Q,z_a;\omega). \quad (33)$$

The wavefield $\widehat{R}_f$ can be interpreted as reflection data, in the absence of interactions with the overburden. As illustrated in Figure 3, $\widehat{R}_f$ indeed does not contain internal multiples from the overburden. To retrieve this wavefield, we realize that equation 32 can also be recognized as a Fredholm integral equation of the second kind. We can rewrite this equation in the time domain as

$$\widehat{U}^-(\boldsymbol{\chi}_P,\boldsymbol{\chi}_A;t)=\widehat{R}_f(\boldsymbol{\chi}_P,\boldsymbol{\chi}_A;t)+\{\mathcal{M}(\zeta)\widehat{R}_f\}(\boldsymbol{\chi}_P,\boldsymbol{\chi}_A;t). \quad (34)$$

Here, we defined the following kernel for multidimensional convolution of an arbitrary wavefield $P(\boldsymbol{\chi}_P,\boldsymbol{\chi}_A;t)$ with ζ:

$$\{\mathcal{M}(\zeta)P\}(\boldsymbol{\chi}_P,\boldsymbol{\chi}_A;t) = \int_{-\infty}^{+\infty} d\tau \int_{\Lambda_a} d^2\boldsymbol{\chi}_Q P(\boldsymbol{\chi}_P,\boldsymbol{\chi}_Q;\tau)\zeta(\boldsymbol{\chi}_Q,\boldsymbol{\chi}_A;t-\tau). \quad (35)$$

A Neumann series expansion of equation 34 leads to

$$\widehat{R}_f(\boldsymbol{\chi}_P,\boldsymbol{\chi}_A;t) = \textstyle\sum_{k=0}^{\infty}\{(-\mathcal{M}(\zeta))^k\widehat{U}^-\}(\boldsymbol{\chi}_P,\boldsymbol{\chi}_A;t). \quad (36)$$

Equation 36 is the first main result of this paper. It can be used to compute a data set $\widehat{R}_f$, which is free from interactions with the overburden (see Figure 3). Convergence is once again guaranteed as long as the norms of operators $\mathcal{R}$ and $\mathcal{R}^\star$ are less than one. Using this result requires knowledge of function ζ. To recover this function, we convolve equation 31 with $G_d^{+*}(\boldsymbol{\chi},z_f;\boldsymbol{\chi}_P,z_a;\omega)$ and integrate over $\boldsymbol{\chi}$. After substitution of equations 13 and 14, we find

$$\widehat{U}_m^+(\boldsymbol{\chi}_P,\boldsymbol{\chi}_A;\omega) = \int_{\Lambda_a} d^2\boldsymbol{\chi}_Q \widehat{U}_d^+(\boldsymbol{\chi}_P,\boldsymbol{\chi}_Q;\omega)\zeta(\boldsymbol{\chi}_Q,\boldsymbol{\chi}_A;\omega). \quad (37)$$

Because $\widehat{U}_d^+$ and $\widehat{U}_m^+$ can be computed by the series expansions in equations 26 and 28, the function ζ can be computed by inversion of equation 37. By such inversion, the scattering transmission losses that are encoded in $\widehat{U}_d^+$ are removed from $\widehat{U}_m^+$ and the wavelet $W(\omega)$ is deconvolved.

We will now illustrate the validity of equation 36 with a synthetic 1D experiment. In Figure 4a and 4b, we show the velocity and density of a model with four layers. The reflection data of this model are shown in Figure 4c, in which we convolved with a Ricker wavelet with a peak frequency of 20 Hz. In the data, we pick traveltime $t_2 = 1.5$ s to indicate the overburden, which is indicated by the dashed line. This traveltime corresponds to a horizon Λ_f at $z_f = 1500$ m. Although this depth does not need to be known in practice, we have indicated it in the figure for convenience. We evaluate the first 50 terms in the series in equation 25 (see Figure 4d). As we explained in Figure 1, we have removed internal multiples at the receiver side by this procedure. However, certain internal multiples remain, such as the event that is indicated by the black circle in the figure. By deconvolving the wavefields $\widehat{U}_m^+$ and $\widehat{U}_d^+$ (as obtained by the series in equations 28 and 26), we can obtain ζ (see equation 37). Using ζ and $\widehat{U}^-$, we can compute $\widehat{R}_f$ with equation 36. The results are shown in Figure 4e. As explained by the cartoons in Figure 3, all internal multiples from the overburden have been eliminated by this procedure.

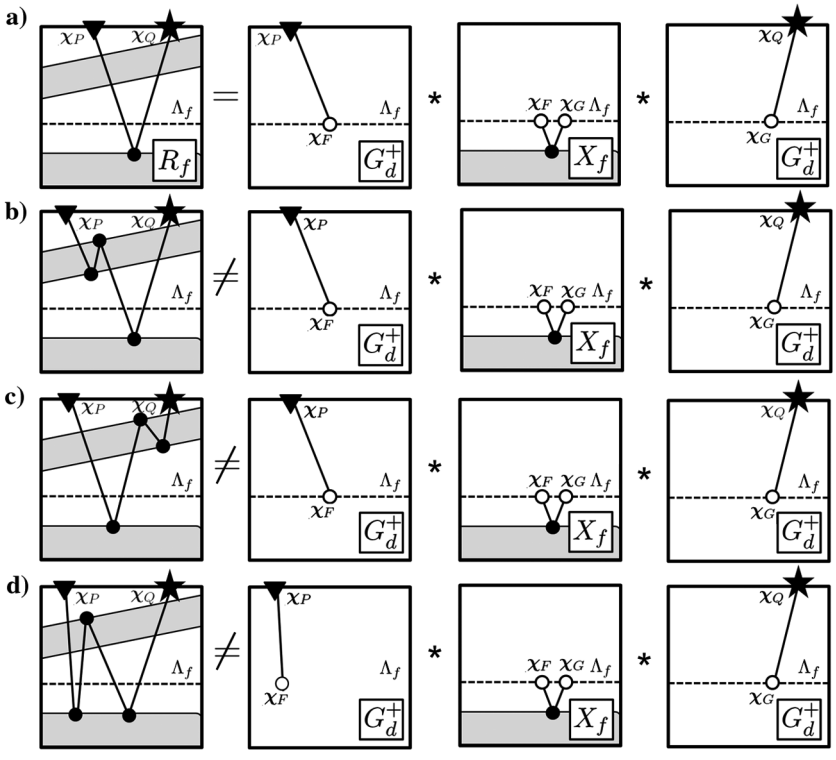

Figure 3. Illustration of equation 33. (a) Primaries that have passed horizon Λ_f are constructed by multidimensional convolution of $G_d^+(\boldsymbol{\chi}_F,z_f;\boldsymbol{\chi}_P,z_a;t)$, $X_f(\boldsymbol{\chi}_F,z_f;\boldsymbol{\chi}_G,z_f;t)$, and $G_d^+(\boldsymbol{\chi}_G,z_f;\boldsymbol{\chi}_Q,z_a;t)$. (b-d) Internal multiples with at least one reflection point above Λ_f are not constructed with equation 33. Hence, these multiples are not part of $R_f(\boldsymbol{\chi}_P,\boldsymbol{\chi}_Q;t)$.

ADAPTIVE SOLUTION

It is obvious that the retrieval of $\widehat{R}_f(t)$ from equation 36 depends on knowledge of the wavefields $\widehat{U}^-(t)$, $\widehat{U}_d^+(t)$, and $\widehat{U}_m^+(t)$. As shown in the previous section, the computation of these wavefields requires the two-way traveltime of a fictitious horizontal reflector at Λ_f and accurate operators $\mathcal{R}$ and $\mathcal{R}^\star$, which should be computed from the recorded reflection data at the acquisition surface. However, as we discussed in the introduction of this paper, the construction of these operators requires complete input data and accurate knowledge of the source signature. The underlying theory does not account for seismic attenuation, which could result in amplitude mismatch when the individual terms in the series of $\widehat{U}^-(t)$, $\widehat{U}_d^+(t)$, and $\widehat{U}_m^+(t)$ (i.e., equations 25, 26, and 28) are added together. As a consequence, the retrieval of $\widehat{R}_f(t)$ through equation 36 will be inaccurate.

Alternatively, we could add the individual components in the series of equation 36 adaptively. By substituting equations 25 and 28 into equation 36, we can derive an expression for adaptive IME. This is the second main result of this paper:

$$\widehat{R}_f(\boldsymbol{\chi}_P;\boldsymbol{\chi}_A;t) \approx \widehat{R}_{f0}(\boldsymbol{\chi}_P,\boldsymbol{\chi}_A;t) - \alpha_1(t) * \widehat{M}_{f1}(\boldsymbol{\chi}_P,\boldsymbol{\chi}_A;t) - \alpha_2(t) * \widehat{M}_{f2}(\boldsymbol{\chi}_P,\boldsymbol{\chi}_A;t). \quad (38)$$

Here, we have defined

$$\widehat{R}_{f0}(\boldsymbol{\chi}_P,\boldsymbol{\chi}_A;t) = \{\Theta_{t_2}^{\infty}\widehat{R}\}(\boldsymbol{\chi}_P,\boldsymbol{\chi}_A;t), \quad (39)$$

as the data after truncation at horizon Λ_f

$$\widehat{M}_{f1}(\boldsymbol{\chi}_P,\boldsymbol{\chi}_A;t) = -\{\Theta_{t_2}^{\infty}\mathcal{R}\Theta_{t_0}^{t_2}\mathcal{R}^\star\Theta_{t_0}^{t_2}\widehat{R}\}(\boldsymbol{\chi}_P,\boldsymbol{\chi}_A;t), \quad (40)$$

as the predicted internal multiples "at the receiver side," and

$$\widehat{M}_{f2}(\boldsymbol{\chi}_P,\boldsymbol{\chi}_A;t) = -\{\mathcal{M}(\mathcal{W}^{-1}\Theta^{\infty}_{t_0}\mathcal{R}\Theta^{-t_0}_{-t_2}\mathcal{R}^{\star}\widehat{\delta})\Theta^{\infty}_{t_2}\widehat{R}\}(\boldsymbol{\chi}_P,\boldsymbol{\chi}_A;t), \tag{41}$$

as the remaining multiples. To arrive at this result, we estimated $\zeta(t)$ from $\widehat{U}^{-}_{m}(t)$ by deconvolving with the wavelet, where we assumed that

$$\zeta(\boldsymbol{\chi}_P,\boldsymbol{\chi}_A;t) \propto \{\mathcal{W}^{-1}\widehat{U}^{+}_{m}\}(\boldsymbol{\chi}_P,\boldsymbol{\chi}_A;t), \tag{42}$$

being an approximation to the inversion that is prescribed in equation 37. Here, and in equation 41, $\mathcal{W}^{-1}$ is an operator to deconvolve with wavelet $W(t)$. Note that the transmission losses are not taken into account by this operation (hence the left and right sides of equation 42 have different amplitudes, explaining the use of the $\propto$ sign). We have ignored terms in the series that require more than three crosscorrelations with the reflection response. As a consequence of the missing terms and the approximation that is introduced in equation 42, the amplitudes of the predicted internal multiples $\widehat{M}_{f1}$ and $\widehat{M}_{f2}$ are incorrect. We aim to compensate for this mismatch by matching filters α_1 and α_2 in equation 38. In this paper, we parameterize these filters as single scalars that are found by minimizing the ℓ_2-norm of the output gathers of $\widehat{R}_f$ in equation 38. Here, we aim to address the most dominant (first order) internal multiples in the data only. However, because the amplitude mismatch can be nonstationary, it might be useful to implement matching filters in sliding windows in the time domain, as typically applied in other IME schemes (Verschuur and Berkhout, 2005). These filters may also compensate for other deficiencies that might occur as a consequence of inaccurate source signature deconvolution, remnants of source/receiver ghosts, seismic attenuation, and data incompleteness.

To illustrate the adaptive procedure, we apply equation 38 to the synthetic model that was evaluated in Figure 4a and 4b. The recorded $\widehat{R}(t)$ and truncated data $\widehat{R}_f(t)$ are shown in Figure 5a and 5b. In Figure 5c and 5d, we display the predicted multiples $\widehat{M}_{f1}(t)$ and $\widehat{M}_{f2}(t)$. These wavefields have been scaled with scalars α_1 and α_2, which are found by minimizing the ℓ_2-norm of $\widehat{R}_f(t)$, as computed in equation 38. In Figure 5e, we show the truncated data, after the predicted multiples have been subtracted. Note that the dominant internal multiple from the overburden, arriving at $t = 1.8$ s, has been subtracted well. However, as the 50 terms of the series that were evaluated in Figure 4 have been truncated with the current procedure, it is not possible to find matching filters for complete elimination of all internal multiples. Hence, the prediction result is not optimal and weaker internal multiples, as indicated by the black circles in Figure 5e, remain present in the output gather. This could be overcome by using nonstationary filters (Fomel, 2006).

INTERPRETATION

To understand the proposed IME process, we interpret the involved multidimensional crosscorrelations by subtracting traveltimes along common raypaths at the stationary points of the underlying integrals. This is an interpretation that is commonly used in seismic interferometry (Schuster, 2009), which is also well-known in the field of IME (Ikelle, 2006) and Marchenko redatuming (van der Neut et al., 2015a). In Figure 6a and 6b, we show how the internal multiples "at the receiver side" are predicted by $\widehat{M}_{f1}$ through the crosscorrelations of three primary reflections. It follows from Figure 6c and 6d how the remaining multiples are predicted by $\widehat{M}_{f2}$ through a similar process.

In all cases, the mechanism for the internal multiple retrieval is closely related to that from other IME schemes, such as the method of Jakubowicz (1998), the ISS (Weglein et al., 1997), the work of Ten Kroode (2002), and source-receiver interferometry (Löer et al., 2016). In each of these methodologies, the data are crosscorrelated twice to retrieve internal multiple reflections. Although this double crosscorrelation process does predict all first-order internal multiples in the data, spurious events and copies of the primary reflections are also created. To avoid the retrieval of these unwanted quantities, particular truncations should be applied. These truncations are often designed, such that the so-called "lower-higher-lower" (LHL) condition is obeyed, meaning that the second reflection point should always be located higher than the first and third reflection points for an event to be a (first-order) internal multiple. In the term $\widehat{M}_{f1}$ that is described in equation 40, the required truncations are imposed in a way that is closely related to the multiple elimination scheme of Ten Kroode (2002) and Löer et al. (2016), which can be derived from source-

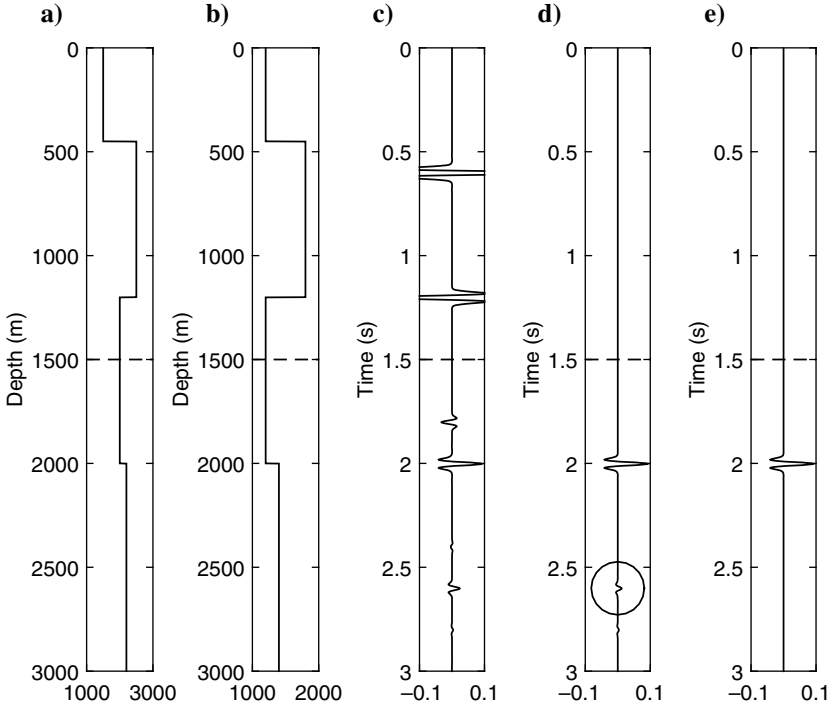

Figure 4. Illustration of equation 36, the first main result of this paper. (a) Velocity model (in m/s) and (b) density model (in kg/m^3). (c) Reflection data $\widehat{R}(t)$. (d) Wavefield $\widehat{U}^{-}(t)$ after applying equation 25. The black circle indicates an internal multiple from the overburden that has not (yet) been eliminated. (e) Wavefield $\widehat{R}_f(t)$ after applying equation 36. All series have been truncated after 50 terms, and ζ has been retrieved by deconvolution of the retrieved wavefields $\widehat{U}^{+}_{m}$ and $\widehat{U}^{+}_{d}$. The dashed lines indicate the depth (in practice unknown) and traveltime t_2 (picked) of horizon Λ_f. We emphasize that only the picked traveltime ($t_2 = 1.5$ s) and the reflection response have been used for the computations.

receiver interferometry and the ISS. Similarly, we can infer relations with the multiple elimination schemes of Jakubowicz (1998) and Van Borselen (2002), when studying the term $\widehat{M}_{f2}$ that is described in equation 41. We will now look at these connections in more detail.

In the ISS, the LHL condition is imposed by truncating integrals in depth. As shown by Ten Kroode (2002), the ISS methodology can be rewritten by truncating integrals in time, under the assumption of traveltime monotonicity. This result has been modified further by Löer et al. (2016), leading to the following first-order prediction mechanism for internal multiples:

$$M_t(\boldsymbol{\chi}_P;\boldsymbol{\chi}_A;t)=\frac{4}{(c\rho)^2}\int_{-\infty}^{+\infty}d\tau'\int_{\Lambda_a}d^2\boldsymbol{\chi}'D(\boldsymbol{\chi}',\boldsymbol{\chi}_P;\tau')\theta(t-\tau'-\epsilon)$$
$$\times\int_{-\infty}^{+\infty}d\tau\int_{\Lambda_a}d^2\boldsymbol{\chi}D(\boldsymbol{\chi}',\boldsymbol{\chi};\tau)\theta(\tau'-\tau-\epsilon)D(\boldsymbol{\chi},\boldsymbol{\chi}_A;t-\tau'+\tau). \tag{43}$$

In this equation, c is the propagation velocity, ρ is the density, and ϵ is a small constant to account for the finite-frequency band of the data (i.e., the source signature). The computed wavefield M_t contains a first-order estimate of internal multiples at time t in the data. One truncation is imposed by the Heaviside function $\theta(t-\tau'-\epsilon)$, enforcing that $D(t-\tau'+\tau)$ will arrive after $D(\tau)$ for any τ. Another truncation is imposed by the Heaviside function $\theta(\tau'-\tau-\epsilon)$, enforcing that $D(\tau')$ will arrive after $D(\tau)$ for any τ. Together, these truncations ensure that the LHL condition is always satisfied.

Note that we can rewrite equation 40 as

$$\widehat{M}_{f1}(\boldsymbol{\chi}_P;\boldsymbol{\chi}_A;t)=\theta(t-t_2)\int_{-\infty}^{+\infty}d\tau'$$
$$\times\int_{\Lambda_a}d^2\boldsymbol{\chi}'R(\boldsymbol{\chi}',\boldsymbol{\chi}_P;\tau')\theta(t-\tau'-\epsilon)$$
$$\times\int_{-\infty}^{+\infty}d\tau\int_{\Lambda_a}d^2\boldsymbol{\chi}R(\boldsymbol{\chi}',\boldsymbol{\chi};\tau)\theta(t_2-(t-\tau'+\tau))$$
$$\times\widehat{R}(\boldsymbol{\chi},\boldsymbol{\chi}_A;t-\tau'+\tau), \tag{44}$$

where ϵ accounts for finite frequency effects. This result is similar but not identical to equation 43. The difference between both equations is a consequence of the different objectives of the IME schemes. Ten Kroode (2002) and Löer et al. (2016) aim to remove all reflections that originate from a subsection of the data that is truncated at $t-\epsilon$, where t is the output time. Because the truncation is applied just before the output time, the primaries are preserved. However, all internal multiples with delay time $>\epsilon$ are removed. In our scheme, we remove all reflections that originate from a subsection of the data that is truncated at t_2. This includes the primaries that arrive before t_2 and internal multiples before, at, and after t_2. Hence, the truncations of Ten Kroode (2002) and Löer et al. (2016) depend only on the output traveltime t, whereas the truncations in our scheme are fixed by our choice for t_2. To see this, we could substitute $t_2=t-\epsilon$ into equation 44. After this operation, the first Heaviside function on the right side becomes redundant and the result can be written as

$$\widehat{M}_{f1}(\boldsymbol{\chi}_P;\boldsymbol{\chi}_A;t)=\int_{-\infty}^{+\infty}d\tau'\int_{\Lambda_a}$$
$$\times d^2\boldsymbol{\chi}'R(\boldsymbol{\chi}',\boldsymbol{\chi}_P;\tau')\theta(t-\tau'-\epsilon)$$
$$\times\int_{-\infty}^{+\infty}d\tau\int_{\Lambda_a}d^2\boldsymbol{\chi}R(\boldsymbol{\chi}',\boldsymbol{\chi};\tau)\theta(\tau'-\tau-\epsilon)$$
$$\times\widehat{R}(\boldsymbol{\chi},\boldsymbol{\chi}_A;t-\tau'+\tau). \tag{45}$$

This equation is identical to equation 43, apart from the scaling factor $4/(c\rho)^2$, which can be attributed to the different normalization of D (see Ten Kroode, 2002; Löer et al., 2016) and the reflection data R as defined in this paper. The third term $\widehat{M}_{f2}$ in equation 38 vanishes when evaluated at $t=t_2+\epsilon$. Hence, equation 45 or 43 is sufficient for a first-order estimate of all internal multiples in this case, as also demonstrated by Löer et al. (2016).

Based on this observation, it is not hard to see how the scheme of Löer et al. (2016) could be extended to remove all internal multiples at traveltime t with correct amplitudes. By substituting equation 25 into equation 36 and evaluating the result at $t_2=t-\epsilon$, we find only the following terms with nonzero contributions:

$$\widehat{R}_t(\boldsymbol{\chi}_P;\boldsymbol{\chi}_A;t)=\textstyle\sum_{k=0}^{\infty}\{\mathcal{R}\Omega_t^k\widehat{\delta}\}(\boldsymbol{\chi}_P;\boldsymbol{\chi}_A;t), \tag{46}$$

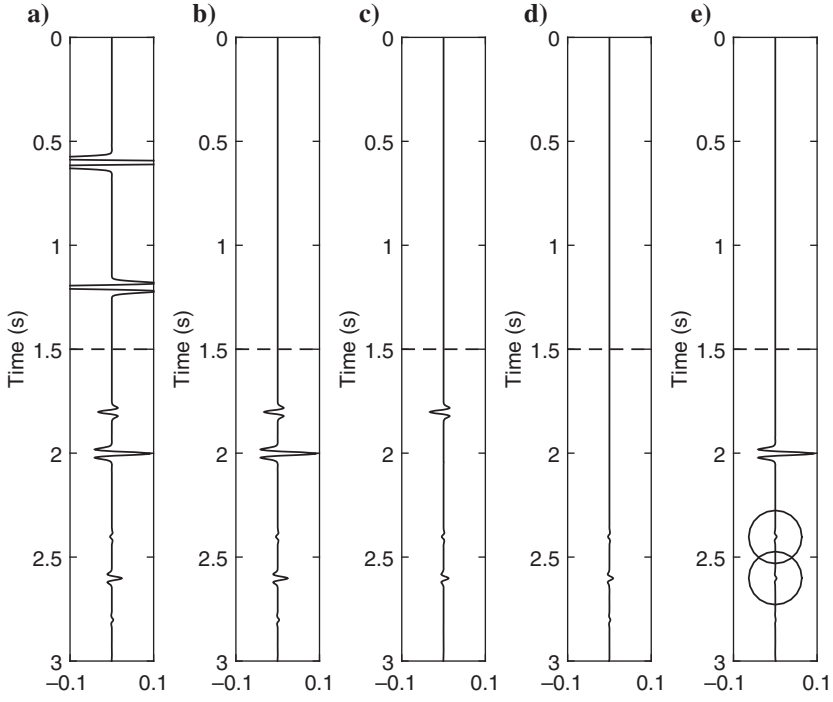

Figure 5. Illustration of equation 38, the second main result of this paper. (a) Reflection data $\widehat{R}(t)$. (b) Truncated data $\widehat{R}_{f0}(t)$ from equation 39. Predicted multiples (c) $\widehat{M}_{f1}(t)$ and (d) $\widehat{M}_{f2}(t)$ from equations 40 and 41 after applying matching filters, which are parameterized by single scalars. (e) Data $\widehat{R}_f(t)$ after the predicted multiples have been subtracted, following equation 38. The black circles indicate internal multiples from the overburden that have not been completely eliminated.

where the kernel should be truncated at traveltime $t_2 = t - \epsilon$, according to

$$\Omega_t = \Theta_{t_0}^{t-\epsilon}\mathcal{R}^{\star}\Theta_{t_0}^{t-\epsilon}\mathcal{R}. \tag{47}$$

In equation 46, which can be considered as the third main result of this paper, $\widehat{R}_t$ is the data after IME. The first term ($k = 0$) on the right side of equation 46 is the reflection data $\{\mathcal{R}\widehat{\delta}\}(t) = \widehat{R}(t)$ and the remaining terms represent internal multiples that are to be subtracted from the first term. Because Ten Kroode (2002) and Löer et al. (2016) derive their results from the third term of the ISS (where data are crosscorrelated twice), their multiple prediction mechanism corresponds to the second term in equation 46 (where data are also crosscorrelated twice). Ramírez and Weglein (2005) show that ISS-based internal multiple predictions can be improved by adding the fifth term of the ISS (where data are crosscorrelated four times) to the third term. Hence, the fifth term of the ISS seems closely related to the third term in equation 46 (where data are also crosscorrelated four times). In 2D or 3D, operator $\Theta_{t_0}^{t-\epsilon}$ could be designed by following two-way traveltime surfaces, which can be computed for any traveltime and offset in the data, using for instance stacking velocities. Although this is considered a useful topic for further research, it reaches beyond our present scope.

As an illustration, we evaluate the series in equation 46 on the model that was presented earlier in Figure 4a and 4b. The first term of the series ($k = 0$) is shown in Figure 7a. Note that this term is equivalent to the recorded reflection data. In Figure 7b, we show the second term of the series ($k = 1$). As explained by Löer et al. (2016), this term contains all internal multiples with erroneous amplitudes. Rather than adding this contribution adaptively to the first term, as suggested by Löer et al. (2016), we may evaluate more terms from the series, obviating the need for adaptive filters. The next three terms are shown in Figure 7b and 7d. In Figure 7e, we show the result after adding the first four terms of the series together. Note that the three primary reflections that are present in the data have survived the procedure, whereas all internal multiples have been effectively removed. This result demonstrates the validity of equation 46 for IME.

In this paper, we have truncated the data at the selected traveltime surface t_2 of the overburden, rather than just before the output time at $t - \epsilon$. Hence, there is an additional term $\widehat{M}_{f2}$ in equation 38, which predicts internal multiples that have crossed the interface Λ_f to arrive at $t > t_2$. The construction of these multiples is demonstrated in Figure 6c and 6d. It is observed that the mechanism in Figure 6d is closely related to the scheme of Van Borselen (2002), who derives his results from the method of Jakubowicz (1998). In the scheme of Van Borselen (2002), all multiples that have crossed the horizon Λ_f (which is referred to as a pseudoboundary) are also predicted by a double crosscorrelation process and particular truncations. These truncations ensure that the first and third reflection points are located below Λ_f, whereas the second reflection point is located above this horizon. To ensure that all internal multiples are removed from the data, a scan should be made over various horizons Λ_f in a top-down approach. In our methodology, such a scan is not required because all internal multiples that are described in Figure 6 are predicted at once, given that $\widehat{M}_{f1}$ and $\widehat{M}_{f2}$ are evaluated in equation 38. Hence, our method has the potential to reduce the computation time for IME below a single target horizon by a factor of $N_h/2$, where N_h is the number of horizons above the target horizon (expressed in two-way traveltime) that should be evaluated by the other algorithms. The factor $1/2$ is included because we have to compute terms $\widehat{M}_{f1}$ and $\widehat{M}_{f2}$ in equation 38, rather than one term as in the other methods.

SIMPLE SYNTHETIC EXAMPLE

We will test the IME scheme that is described in equation 38 on two synthetic data sets and field data. For the first test, which we discuss in this section, we use a synthetic model that has been described in more detail by Wapenaar et al. (2014b). The propagation velocity is shown in Figure 8. At the acquisition surface, seismic data are modeled with 301 sources and 301 receivers on a fixed spread with a spacing of 10 m. Absorbing boundary conditions are applied at the top of the model, and the direct wave has been removed. The reflection response has been modeled with a flat frequency spectrum for an optimal design of the operators $\mathcal{R}$ and $\mathcal{R}^{\star}$. The data $\widehat{R}(\boldsymbol{\chi}_P, \boldsymbol{\chi}_A; t)$ have been computed by convolving this

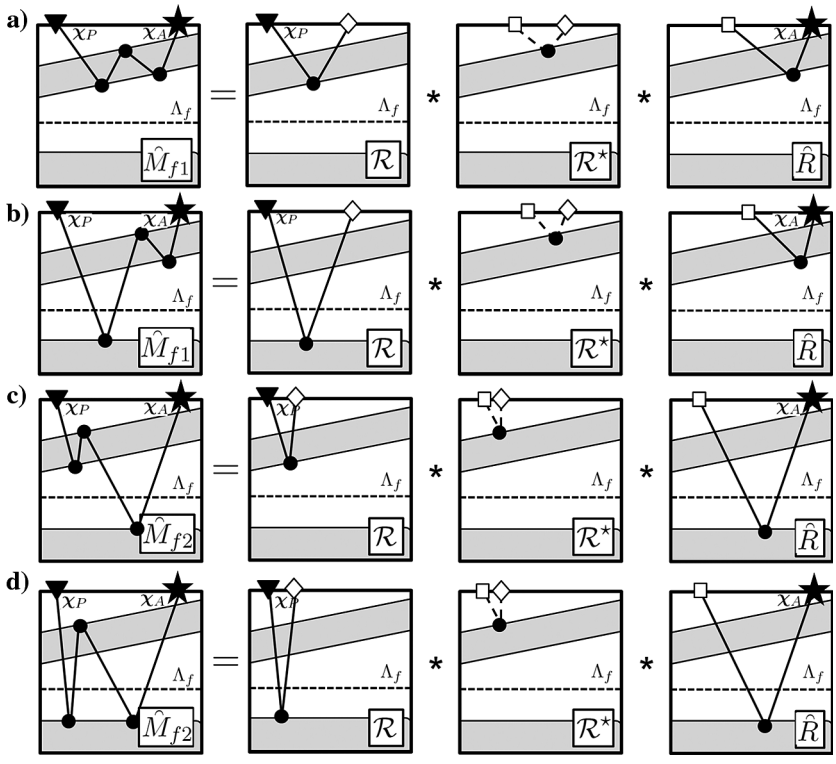

Figure 6. Illustration of the construction of the first-order multiples. In (a and b), we show how multiples at the "receiver side" are constructed by evaluation of $\widehat{M}_{f1}$ in equation 40. In (c and d), we show how other multiples are constructed by evaluation of $\widehat{M}_{f2}$ in equation 41. In each case, the data are crosscorrelated twice and particular truncations are being applied in the time domain. Solid raypaths denote positive traveltimes. Dashed raypaths denote negative traveltimes, which are subtracted from the positive traveltimes. The white squares and diamonds are stationary points at the surface that contributed to the underlying integrals.

reflection response with a Ricker wavelet with a peak frequency of 20 Hz.

In Figure 9a, we show an arbitrary shot record of the reflection data $\widehat{R}(\boldsymbol{\chi}_P,\boldsymbol{\chi}_A;t)$. In these data, we pick a two-way traveltime surface $t_2(\boldsymbol{\chi}_P,\boldsymbol{\chi}_A)$ of a fictitious reflector that is located somewhere below the overburden, as indicated by the dashed white line in the figure. To emphasize our relative independence on velocity information, we have picked this surface not very accurately, slightly above the first reflector of our interest, roughly following the moveout of this reflector. With the dashed white line in Figure 8, we interpret the picked horizon as belonging to a fictitious reflector at some depth level z_f below the overburden. Although t_2 determines which internal multiples are to be removed, the accuracy of our picks seems not very important for the robustness of the algorithm. This is not the case for traveltime surface t_0 that will be discussed in the following paragraph.

We partition the data into two subsets. In the first subset, we remove all information after t_2. Because the data are causal and the direct wave has been removed, all gathers are empty before t_0, making the first subset equivalent to $\{\Theta_{t_0}^{t_2}\widehat{R}\}(\boldsymbol{\chi}_P,\boldsymbol{\chi}_A;t)$, which should enter through equation 40. In the second subset, we remove all information before t_2. This subset is equivalent to $\{\Theta_{t_2}^{\infty}\widehat{R}\}(\boldsymbol{\chi}_P,\boldsymbol{\chi}_A;t)$, which is the wavefield that should enter through equation 41. To conduct the remaining computations that are required for the evaluation of equation 38, t_0 should be known. To determine this traveltime surface, we apply the filter $\mathcal{R}^\star$ to the first subset. In Figure 9b, we display an arbitrary shot of the resulting wavefield $\{\mathcal{R}^\star\Theta_{t_0}^{t_2}\widehat{R}\}(\boldsymbol{\chi}_P,\boldsymbol{\chi}_A;t)$. We find a strong event at the origin, being a superposition of all autocorrelated events from the overburden. This event can be interpreted as the update of $U_d^+(-t)$, which is given by the second term in equation 26. For the IME scheme to work, this update should be excluded from the update of $\widehat{v}_m^+(t)$ (appearing at $t>0$). This is done by selecting a traveltime surface $t_0(\boldsymbol{\chi}_P,\boldsymbol{\chi}_A)$ just after the event in the origin, as indicated by the dashed white line in Figure 9b. Although this procedure is not hard to apply in an automated fashion, we emphasize the importance of the accuracy of this truncation. As in conventional Marchenko redatuming, we cannot process internal multiples beyond a certain resolution, which is determined by the frequency content of the data (Slob et al., 2014). Within our procedure, the resolution is determined by our choice for t_0. This traveltime surface should be sufficiently far from the origin to exclude the updates of $\widehat{U}_d^+(-t)$, but it should be sufficiently close to the origin to address internal multiples from fine layers. The optimal choice for t_0 is a trade-off that depends on the frequency content, data quality, and geology. In practice, it can be useful to apply a taper for the required truncations at t_0. In this example, we have used a short taper of two time samples only.

Now that we have determined the traveltime surfaces t_2 and t_0, we can compute all three terms in equation 38. In Figure 10a, we show a common-offset section of the truncated input data $\widehat{R}_{f0}$ at 500 m offset. We have indicated the primary reflections of interfaces 1–5, which we also pointed out in the model in Figure 8. A strong imprint of internal multiples can be observed. In Figure 10b, we show the same section, after IME has been applied with equation 38. Note that the primaries 1–5 have been well-preserved by the operation, whereas various internal multiples have been removed. Below these interfaces, however, internal multiples (from the overburden and interfaces 1–5) have not been eliminated completely. This is a consequence of truncating the series and relying on global matching filters. To improve this performance, one could try to include more

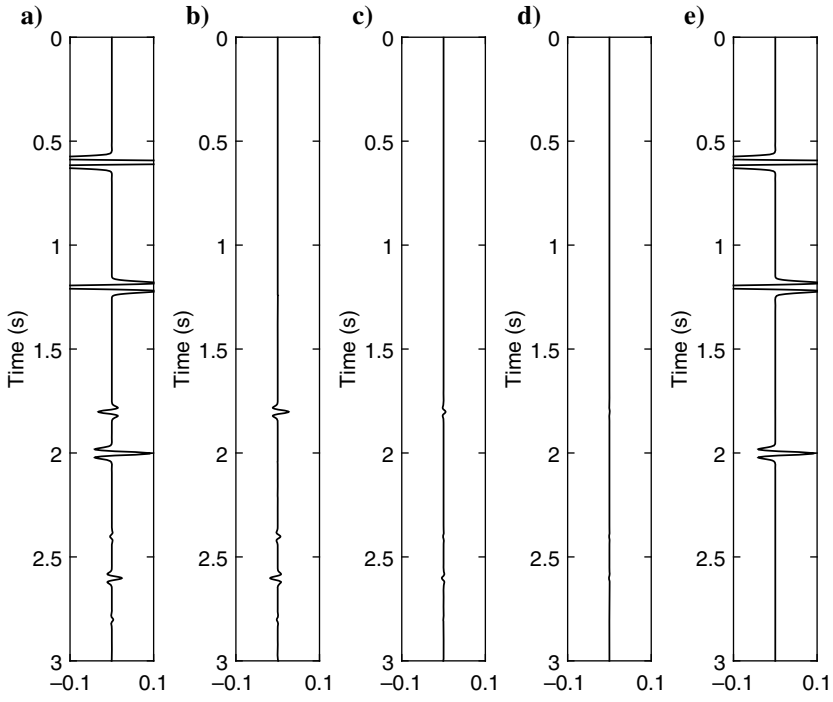

Figure 7. Illustration of equation 46, the third main result of this paper. (a) Reflection data $\widehat{R}(t)$, being equivalent to the first term of the series ($k=0$). (b) Second ($k=1$), (c) third ($k=2$), and (d) fourth ($k=3$) terms of the series. (e) Result $\widehat{R}_t(t)$ after the first four terms of the series have been added together.

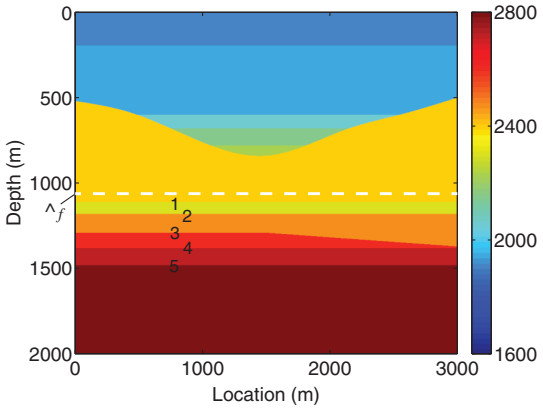

Figure 8. Synthetic model for the simple synthetic example. The colorbar represents the propagation velocity in meters per second. The dashed line represents a fictitious horizon Λ_f. Interfaces 1–5 have been marked.

terms of the series and to apply the matching filters either in local sliding windows (Verschuur and Berkhout, 2005) or by nonstationary regression (Fomel, 2006). The subtracted internal multiples $\widehat{M}_{f1}$ and $\widehat{M}_{f2}$, which are described by the second and third terms in equation 38, are displayed in Figure 10c and 10d, respectively. Here, we have parameterized the matching filters by single scalars, which are found by minimizing the least-squares norm of the output gather $\widehat{R}_{f0}(t)$. Note that the reflectors above Λ_f are relatively strong compared with the reflectors below Λ_f in this example. Hence, the dominant internal multiples are of the kind that is described in Figure 6a. Because these internal multiples are all predicted by $\widehat{M}_{f1}$ rather than by $\widehat{M}_{f2}$, the predictions of $\widehat{M}_{f1}$ (Figure 10c) are relatively stronger than those of $\widehat{M}_{f2}$ (Figure 10d).

The results can also be analyzed in the common-midpoint (CMP) domain. As an example, we pick the CMP location at 1000 m and display the data as a function of offset in Figure 11. As expected, the predicted internal multiples have different moveouts than the primary reflections. This observation is even more clear after NMO correction (see Figure 12). Note the strong interference of the primaries and internal multiples at the time interval [1 and 1.4 s]. This interference could easily obstruct velocity analysis, as we illustrate with the semblance plots for this interval, which are shown in Figure 13. The dashed black line in this figure represents the semblance picks that were used for the NMO correction in Figure 12, which we assume to be representative for the primary reflections in the data. Note the strong obstructions that are caused by the internal multiples in Figure 13a, which have been almost completely eliminated in Figure 13c. It should be remembered that we have used no velocity information for this procedure other than the estimates of the traveltime surfaces t_0 (determining the minimum delay time for an event to be considered an internal multiple) and t_2 (defining what we consider as overburden).

COMPLEX SYNTHETIC EXAMPLE

In the second example, we make use of a model that was provided by Saudi Aramco (see Figure 14). This model contains a few difficult features, such as a varying thin layer (indicated as layer x in the figure) in the shallow subsurface and various pinch-outs, causing diffraction-like phenomena. From a theoretical point of view, we know that both phenomena cause fundamental problems for using the multidimensional Marchenko equation because the underlying causality arguments that we used to define the truncation times are no longer satisfied (van der Neut et al., 2015a). Despite these limitations, we will show in this section that the proposed methodology is robust and that a significant portion of internal multiples can be eliminated in this environment with the help of equation 38.

The data are modeled with a Ricker wavelet with 15 Hz peak frequency. Operators $\mathcal{R}$ and $\mathcal{R}^\star$ have been obtained by stabilized deconvolution of the data with the (known) source wavelet. The acquisition array consists of 301 sources and 301 receivers on a fixed spread with 10 m spacing. To avoid truncation artifacts, the first and last

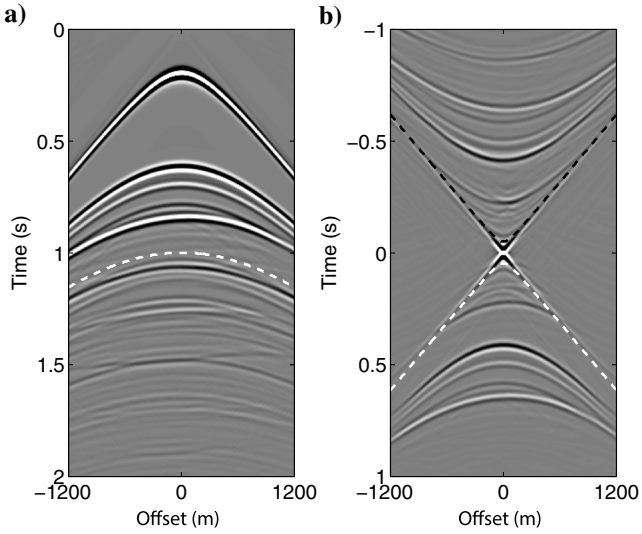

Figure 9. (a) Shot record of the recorded data $\widehat{R}(\chi_P,\chi_A;t)$ with fixed $\chi_A = 0$ m. The white curve depicts a two-way traveltime curve $t_2(\chi_P,\chi_A)$ that we picked in this record just above the earliest reflector of our interest. Amplitudes have been clipped at 10% of the strongest arrival in the gather. (b) Shot record of the crosscorrelated data $\{\mathcal{R}^\star\Theta^{t_2}_{t_0}\widehat{R}\}(\chi_P,\chi_A;t)$ with fixed $\chi_A = 0$ m. The white curve depicts the traveltime curve of $t_0(\chi_P,\chi_A)$ that we picked in this records to remove the contributions at the origin. The black curve depicts the time-reversed traveltime curve $-t_0(\chi_P,\chi_A)$. Amplitudes have been clipped at 5% of the strongest arrival in the gather.

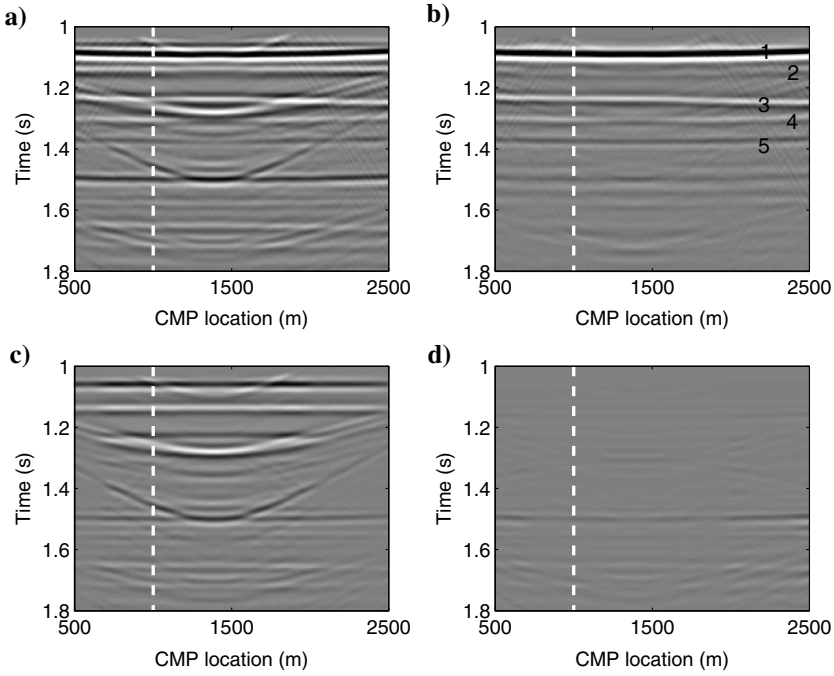

Figure 10. A common-offset gather at 500 m offset, (a) before and (b) after IME. In (c and d), we show the internal multiple predictions of $\widehat{M}_{f1}$ and $\widehat{M}_{f2}$, respectively (single scalars have been used for the matching filters α_1 and α_2). Primary reflections from interfaces 1–5 have been marked. All other events are internal multiples. The dashed white line represents the CMP location that is evaluated in Figures 11 and 12. All amplitudes have been clipped at 50% of the strongest arrival in (a).

25 sources of the array have been tapered with a cosine taper. In Figure 15a, we show a shot record of the input data $\widehat{R}(\chi_P,\chi_A;t)$. As in the previous example, we pick a two-way traveltime surface $t_2(\chi_P,\chi_A)$ below the lowest primary reflector of the overburden, following roughly the moveout of this reflector in the CMP domain. This surface is indicated by the dashed white line in the figure. We assume that this traveltime surface corresponds to some fictitious reflector at depth level z_f, which is located somewhere below the overburden, as indicated in Figure 14. Although this boundary is not exactly horizontal, this is not expected to harm the methodology severely. The data are truncated and crosscorrelated to obtain the wavefield $\{\mathcal{R}^\star\Theta^{t_2}_{t_0}\widehat{R}\}(\chi_P,\chi_A;t)$, which is shown in Figure 15b. Although an automatic procedure could be applied here, we have picked the traveltime surface $t_0(\chi_P,\chi_A;t)$ manually, as indicated in the figure. To address the fine layer (indicated as layer x in Figure 14) in the shallow subsurface in the best possible way, we avoid the use of a taper when designing the truncation operators.

Now that the traveltime surfaces t_2 and t_0 have been determined, we can compute the truncated data $\widehat{R}_{f0}$ and subtract the multiple predictions of $\widehat{M}_{f1}$ and $\widehat{M}_{f2}$. For the matching filters, we have used

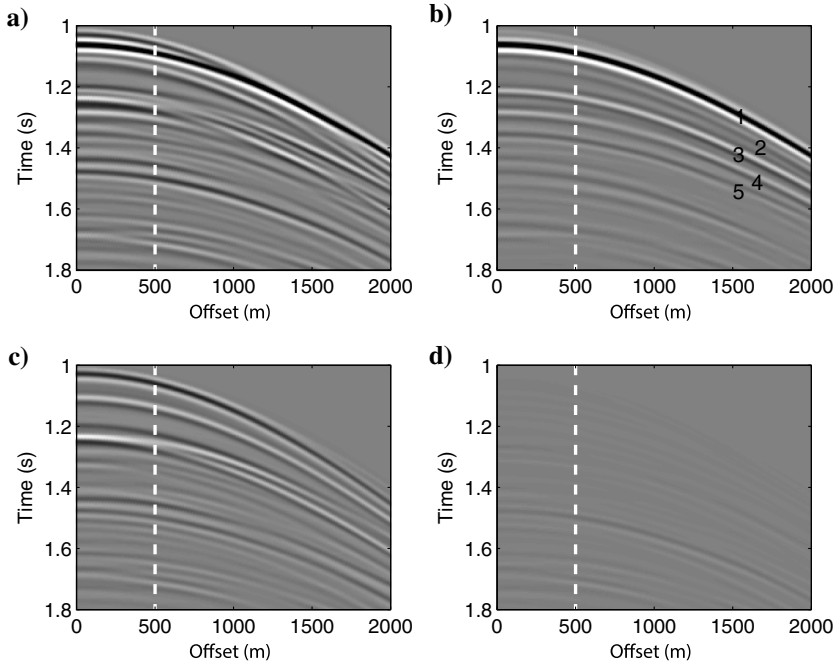

Figure 11. A CMP gather for the CMP location at 1000 m, (a) before and (b) after IME. In (c and d), we show the internal multiple predictions of $\widehat{M}_{f1}$ and $\widehat{M}_{f2}$, respectively (single scalars have been used for the matching filters α_1 and α_2). Primary reflections from interfaces 1–5 have been marked. The dashed white line indicates the offset that is evaluated in Figure 10. All amplitudes have been clipped at 50% of the strongest arrival in (a).

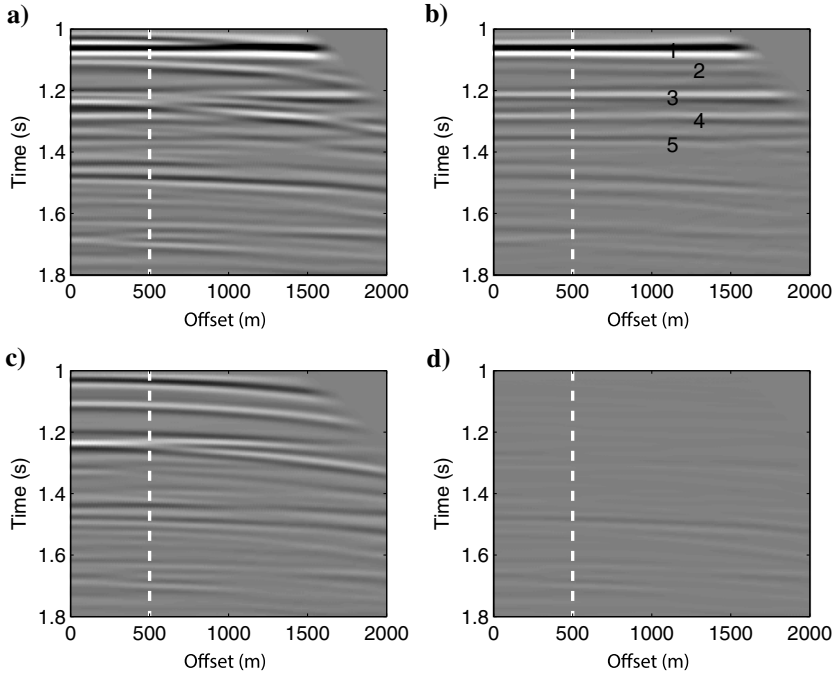

Figure 12. A CMP gather after NMO correction for the CMP location at 1000 m, (a) before and (b) after IME. In (c and d), we show the internal multiple predictions of $\widehat{M}_{f1}$ and $\widehat{M}_{f2}$, respectively (single scalars have been used for the matching filters α_1 and α_2). Primary reflections from interfaces 1–5 have been marked. The dashed white line indicates the offset that is evaluated in Figure 10. All amplitudes have been clipped at 50% of the strongest arrival in (a).

single scalars that were found by minimizing the ℓ_2-norm of the output gather. The result of this operation is shown in Figure 16. Note that most of the events with moderate dips have been subtracted well. However, in some parts of the gather where steeper dips occur (for instance within the black box in the figure), various internal multiples remain. This limitation could be the result of data incompleteness (especially at the left edge of the acquisition array) and the fact that the diffractionlike features are not obeying some of the causality arguments that undergird the multidimensional Marchenko equation (van der Neut et al., 2015a). However, despite these limitations, we observe that all predicted multiples (also within the black box) correspond to physical events in $\widehat{R}_{f0}$. Hence, it might be possible to improve the performance of our algorithm with more sophisticated matching filters.

In Figure 17, we visualize the results as a function of offset for a CMP at 2000 m. As expected, the predicted multiples have a different moveout than the primary reflections from interfaces 1–3, which are indicated in the figure. We observe that internal multiples have been removed at small offsets, whereas the method has failed at larger offsets. It is well-known that the retrieval of internal multiples requires particular stationary points to be sampled by the acquisition array (van der Neut et al., 2015a). Because this array is truncated (with a relatively long taper of 25 sources), some retrieved events can be inaccurate, hampering the multiple subtraction process, especially at higher offsets.

Despite these limitations, the consequences for velocity analysis are significant. This is demonstrated in Figure 18a–18c, showing semblance plots of the input data, the predicted internal multiples and the output data. Although the semblances of interfaces 1–3 can easily be observed, also in Figure 18a, the gather is overwhelmed by stronger internal multiples (especially in the zone that is indicated by the dashed black ellipse). Note that these multiples have been largely removed in Figure 18c, whereas the constructive interference of the primary reflections 1–3 has been improved.

As in the previous example, the gather $\widehat{M}_{f1}$ contains relatively more internal multiples than $\widehat{M}_{f2}$. This has been explained before, given the fact that the dominant internal multiples are of the type that is illustrated in Figure 6a (where all reflection points are located above Λ_f). This is a direct consequence of our choice for the truncation surface t_2, determining which part of the overburden we choose to be eliminated (and how). To illustrate this, we reprocess the data for an alternative traveltime surface t_2', being the upper white curve in Figure 15a. It is assumed that t_2' corresponds to a fictitious reflector at a relatively shallow boundary Λ_f', which is indicated approximately in Figure 14. Note that this horizon varies smoothly with CMP location and that it intersects with medium dis-

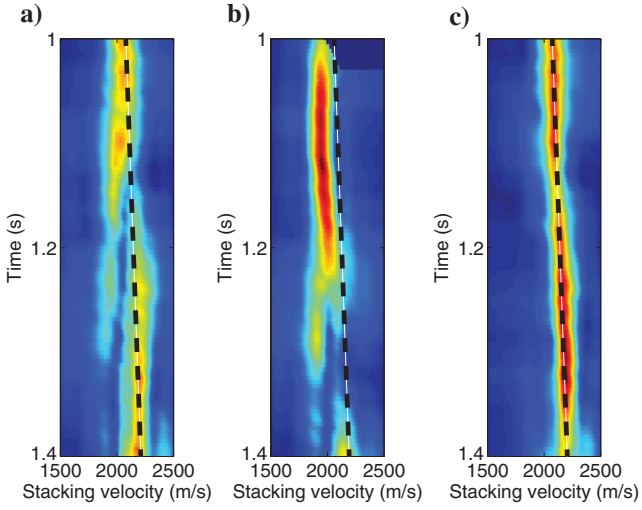

Figure 13. Semblance plot of (a) the input data, (b) the predicted internal multiples, and (c) the data after IME. The dashed black line is the trend that we picked for the NMO correction in Figure 12.

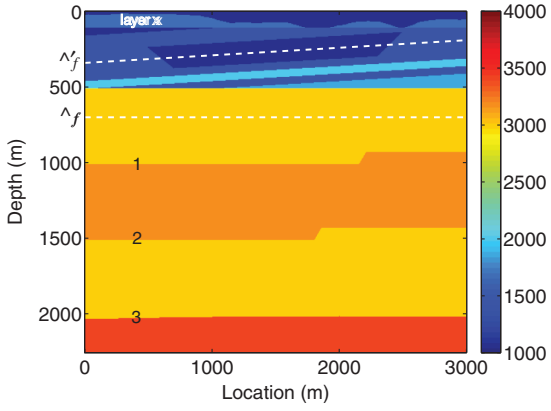

Figure 14. Synthetic model for the complex synthetic example. The colorbar represents the propagation velocity in meters per second. The dashed lines represent two fictitious horizons Λ_f (lower surface) and Λ_f' (upper surface). Interfaces 1–3 and layer x have been marked.

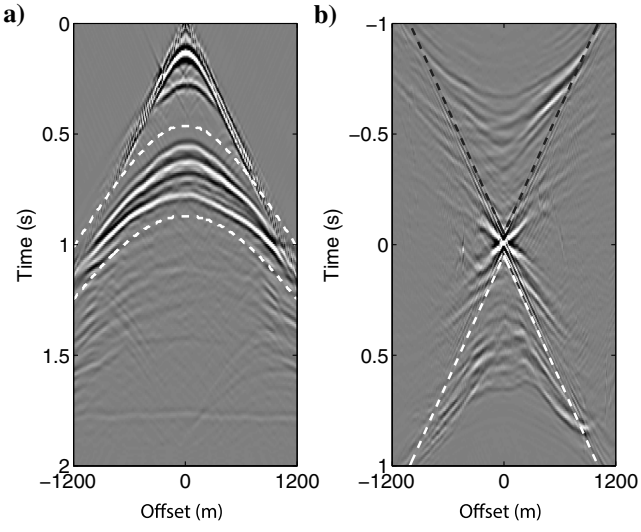

Figure 15. (a) Shot record of the recorded data $\widehat{R}(\chi_P,\chi_A;t)$ with fixed $\chi_A = 0$ m. The lower white curve depicts a two-way traveltime curve $t_2(\chi_P,\chi_A)$ that we picked in this record just above the earliest reflector of our interest. The upper white curve depicts an alternative traveltime curve $t_2'(\chi_P,\chi_A)$. Amplitudes have been clipped at 10% of the strongest arrival in the gather. (b) Shot record of the crosscor related data $\{\mathcal{R}^\star\Theta_{t_0}^{t_2}\widehat{R}\}(\chi_P,\chi_A;t)$ with fixed $\chi_A = 0$ m. The white curve depicts the traveltime curve of $t_0(\chi_P,\chi_A)$ that we picked in this record to remove the contributions at the origin. The black curve depicts the time-reversed traveltime curve $-t_0(\chi_P,\chi_A)$. Amplitudes have been clipped at 5% of the strongest arrival in the gather.

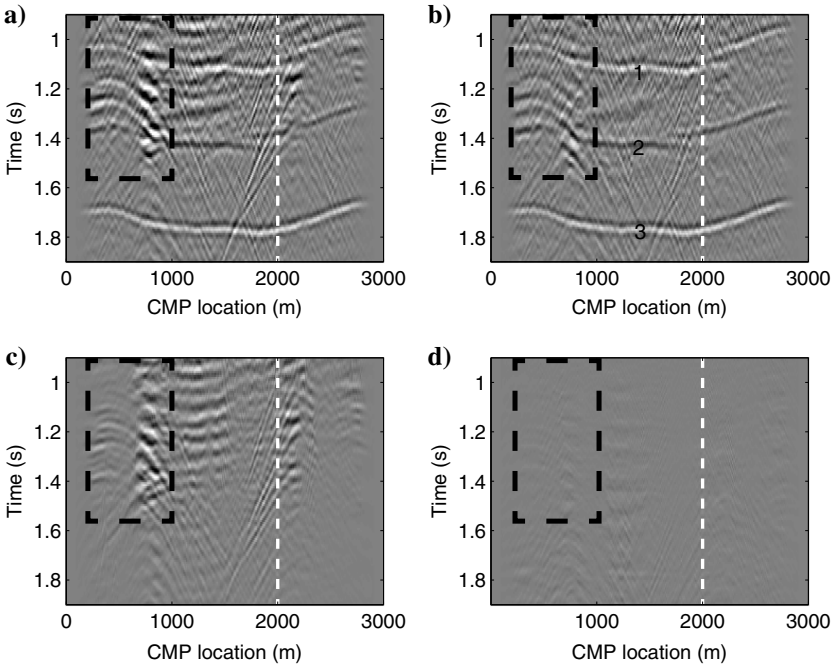

Figure 16. A common-offset gather at 200 m offset, (a) before and (b) after IME. In (c and d), we show the internal multiple predictions of $\widehat{M}_{f1}$ and $\widehat{M}_{f2}$, respectively (single scalars have been used for the matching filters α_1 and α_2). Primary reflections from interfaces 1–3 have been marked. The dashed white line represents the CMP location that is evaluated in Figure 17. The dashed black box indicates an area, where the multiple elimination process is incomplete. All amplitudes have been clipped at 50% of the strongest arrival in (a).

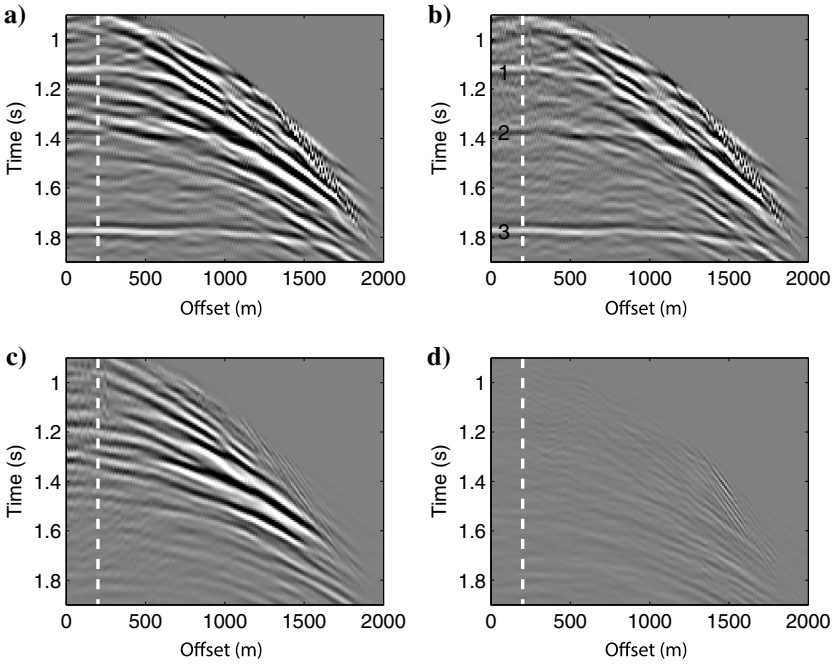

Figure 17. A CMP gather for the CMP location at 2000 m, (a) before and (b) after IME. In (c and d), we show the internal multiple predictions of $\widehat{M}_{f1}$ and $\widehat{M}_{f2}$, respectively (single scalars have been used for the matching filters α_1 and α_2). Primary reflections from interfaces 1–3 have been marked. The dashed white line indicates the offset that is evaluated in Figure 16. All amplitudes have been clipped at 25% of the strongest arrival in (a).

continuities. Although the exact consequences of these observations are still to be explored, they do not seem to harm the methodology. We recompute all gathers with this renewed truncation time and show the results in the CMP domain in Figure 19. Note that the IME process has once more been successful at near offsets, whereas it fails at higher offsets. However, unlike in Figure 17, the dominant internal multiples are in gather $\widehat{M}_{f2}$ rather than in $\widehat{M}_{f1}$. To understand this observation, we should realize that because level Λ_f' is relatively shallow, most internal multiples are of the type that is illustrated in Figure 6d (where the first and last reflection points are located below Λ_f'). This type of internal multiples is predicted by $\widehat{M}_{f2}$ rather than by $\widehat{M}_{f1}$. In fact, evaluating the predictions for different traveltime surfaces t_2 could be used as a diagnostic tool for the origin of the various internal multiples in the data. Such a tool might be especially relevant in cases where different types of internal multiples are significantly interfering.

MARINE DATA TEST

In this section, we will test the proposed algorithm on 2D streamer data. For more information on these data, see Abtheyab et al. (2013). For our test, we select a relatively simple part of the data, covering 4000 m at the surface. The data have been recorded with 25 m source spacing and 12.5 m receiver spacing. By source-receiver reciprocity and interpolation on the source side, we regularize the recorded data to a fixed spread with 321 source and receiver locations with 12.5 m spacing. Cosine tapers have been applied to the first and last 25 source locations. We interpolated the missing near offsets by NMO correction and cubic spline interpolation, following Verschuur (1991). Free-surface multiples have been removed (although remnants may occur in the data) and an estimate of the source signature has been deconvolved to obtain the operators $\mathcal{R}$ and $\mathcal{R}^\star$. A $\sqrt{t}$ correction has been applied to account for 3D geometric spreading. For illustrative purposes, we have stacked the data after NMO correction in Figure 20a. The overburden is characterized by a package of strong reflectors, which we expect to generate internal multiples deeper in the gathers. These strong shallow reflectors are also evident in an interpolated shot record, which we show in Figure 20b. Below these reflectors, we pick the traveltime surface t_2, which is indicated by the white line in the figure. We assume that this surface corresponds to the two-way traveltime of a fictitious reflector at the depth level of Λ_f, as indicated in Figure 20a. Note that the surface varies smoothly in time as we vary its location, which is not expected to harm the methodology, as long as the causality

properties in Figure 2 are satisfied. As in the previous examples, we have crosscorrelated the truncated data to compute $\{\mathcal{R}^{\star}\Theta_{t_0}^{t_2}\widehat{R}\}(\chi_P, \chi_A; t)$, which is shown in Figure 20c. As indicated by the dashed lines, we have picked a traveltime surface t_0 just after the autocorrelated events in the origin, allowing us to compute the wavefields $\widehat{R}_{f0}$, $\widehat{M}_{f1}$, and $\widehat{M}_{f2}$, as they appear in equation 38.

In Figure 21, we show the truncated input data $\widehat{R}_{f0}$, as well as the predicted multiples $\widehat{M}_{f1}$ and $\widehat{M}_{f2}$. As in the previous examples, we have used single scalars to match the internal multiple predictions to $\widehat{R}_{f0}$. A gain with t has been applied to the output gathers to boost the later arrival times. Further, we have clipped the amplitudes heavily at 10% of the maximum value in $\widehat{R}_{f0}$. Overall, the quality of the predictions in $\widehat{M}_{f1}$ seems better than in $\widehat{M}_{f2}$. Several events match with internal multiples in the input data $\widehat{R}_{f0}$, as indicated by markers 1–3. The match is not perfect, which could be due to seismic attenuation, 3D effects, imperfect source signature deconvolution,

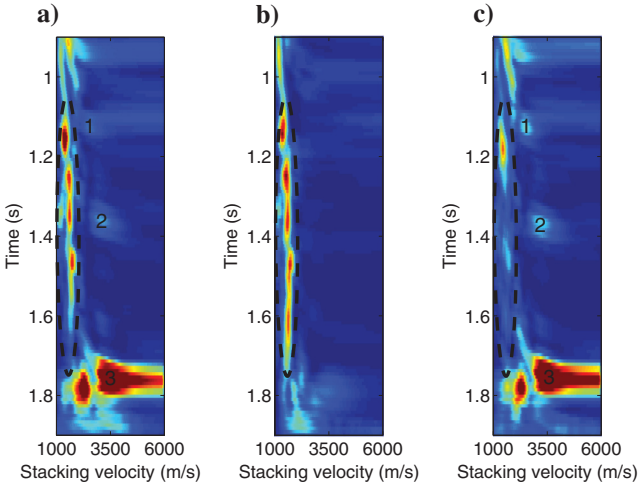

Figure 18. Semblance plot of (a) the input data, (b) the predicted internal multiples, and (c) the data after IME. Contributions from primary reflections 1–3 have been indicated. The dashed black ellipse indicates the contributions of various internal multiples, which have been largely removed by the algorithm.

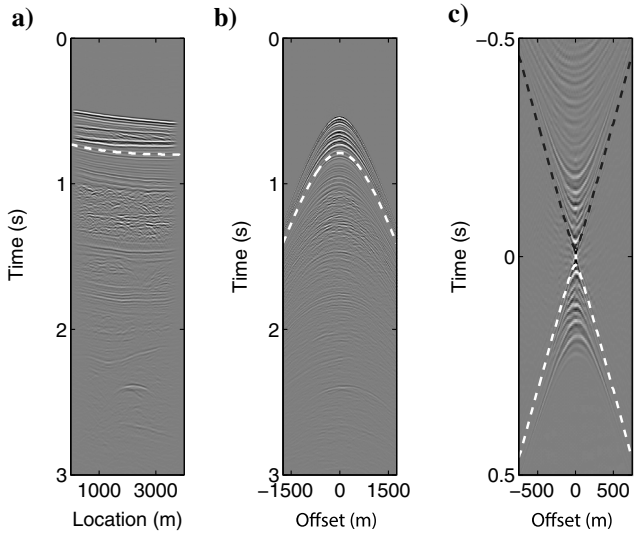

Figure 20. (a) Stack of the field data. The white line indicates boundary Λ_f, defining the depth of the overburden, which we want to eliminate. (b) Shot record of the interpolated data $\widehat{R}(\chi_P, \chi_A; t)$ with fixed $\chi_A = 0$ m. The lower white curve depicts a two-way traveltime curve $t_2(\chi_P, \chi_A)$ that we have picked just below the strongest reflectors in the overburden. (c) Shot record of the crosscorrelated data $\{\mathcal{R}^{\star}\Theta_{t_0}^{t_2}\widehat{R}\}(\chi_P, \chi_A; t)$ with fixed $\chi_A = 0$ m. The white curve depicts the traveltime curve of $t_0(\chi_P, \chi_A)$ that we have picked to remove the contributions at the origin. The black curve depicts the time-reversed traveltime curve $-t_0(\chi_P, \chi_A)$.

Figure 19. A CMP gather for the CMP location at 2000 m, (a) before and (b) after IME. Here, the traveltime surface t_2' (corresponding to a shallow boundary Λ_f') has been used, rather than t_2 (corresponding to the deeper boundary Λ_f). In (c and d), we show the internal multiple predictions of $\widehat{M}_{f1}$ and $\widehat{M}_{f2}$, respectively (single scalars have been used for the matching filters α_1 and α_2). All amplitudes have been clipped at 25% of the strongest arrival in (a).

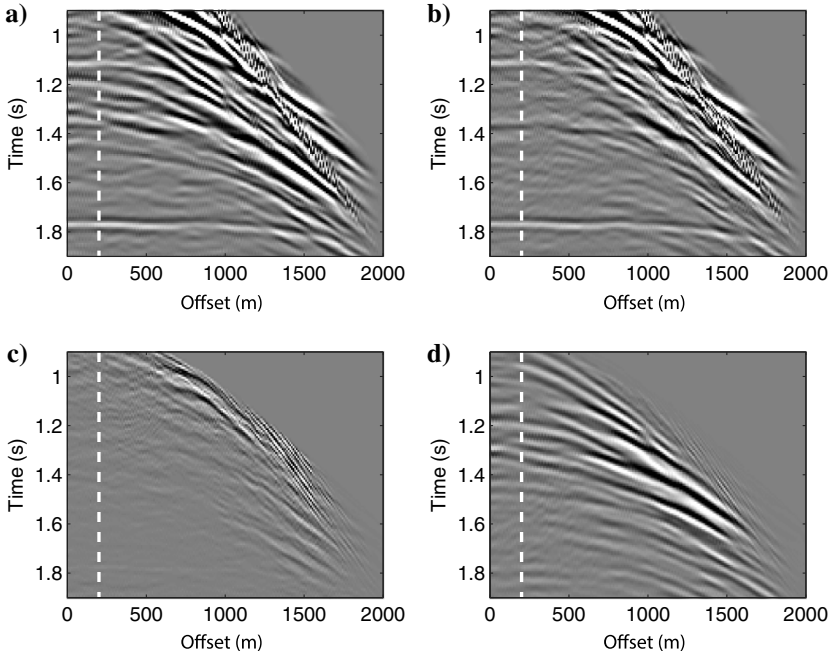

source/receiver ghosts, and other effects that are not accounted for in the theory. We observe correlations between the predictions in $\widehat{M}_{f1}$ and $\widehat{M}_{f2}$ as well, such as indicated by markers 4 and 5. This can be understood intuitively because the multiples that are predicted in Figure 6b and 6c have similar traveltimes when horizontal variations are mild. It should be observed that events 4 and 5, and various other events in the gather, interfere strongly with the primaries, other internal multiples, and the remnants of free-surface multiples. Hence, the assumption that the ℓ_2-norm of the output gathers should be minimized seems unsatisfied for these data and, consequently, we find great difficulty in subtracting the predictions from the input gathers. Here, it should be emphasized that the amplitudes of the predicted multiples are relatively small (remember that the gathers in Figure 21 are strongly clipped).

DISCUSSION

As we have demonstrated with a 1D example, all orders of internal multiples can be removed with equation 36, if a sufficient number of updates are being evaluated. However, because we have to crosscorrelate multiple times with the recorded data, the signal quality tends to degrade in higher order terms (mainly due to incomplete deconvolution of the source signature and the presence of noise in the data), which seems undesirable for robust applications. Moreover, by interpreting each update of the iterative scheme individually (van der Neut et al., 2015a) or by analyzing an arbitrary case study, it can be reasoned that higher order updates play a role mainly to balance amplitudes, rather than to predict unknown arrivals. For these reasons, we have decided to truncate the series and to include only double crosscorrelations with the data. By doing so, we have shown that the first-order internal multiples can be subtracted well with global adaptive filters, but that inaccuracies occur in the amplitudes of higher order multiples and at high offsets, due to the finite acquisition aperture. To overcome these inaccuracies, more accurate and localized matching filters can be implemented,

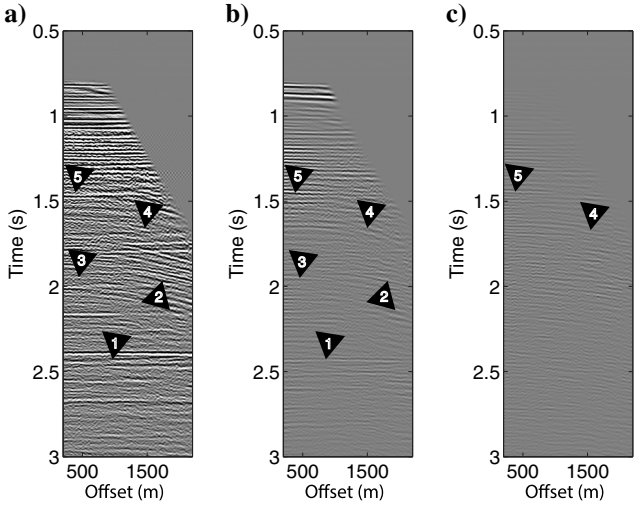

Figure 21. The CMP gathers after NMO correction for the CMP location at 2500 m. (a) The truncated data $\widehat{R}_{f0}$, (b) predicted multiples in $\widehat{M}_{f1}$, and (c) predicted multiples in $\widehat{M}_{f2}$ (single scalars have been used for the matching filters α_1 and α_2). Amplitudes have been clipped at 10% of the strongest arrival in $\widehat{R}_{f0}$ and the gathers have been gained with t. Some events have been indicated by markers 1–5.

following the experiences with equivalent IME algorithms (Verschuur and Berkhout, 2005; Fomel, 2006).

We have mentioned various similarities with existing IME schemes. The derived result is different from the ISS-based schemes of Ten Kroode (2002) and Löer et al. (2016) in the sense that we make use of a selected horizon in the subsurface. It differs from the algorithms of Jakubowicz (1998) and Van Borselen (2002) in the sense that it can be applied at any depth level in the subsurface, without the need for layer stripping. In all schemes, the recorded data are crosscorrelated twice. However, the integral truncations are different. In this paper, we have shown that two types of truncations should be imposed to derive the multidimensional Marchenko equation. Truncation at time t_2 is applied to define an overburden, whereas truncation at time t_0 is applied to define the shortest delay time for an event to be considered an internal multiple. Depending on the frequency band of the data, a reverberation of a thin layer is considered part of the direct wavefield, unless it separates sufficiently in time from this wavefield. Because truncation at t_0 separates the direct wavefield from the internal multiples, it plays an essential role for any multiple elimination scheme to perform well. In the original Marchenko imaging scheme of Wapenaar et al. (2014b), both kinds of truncations are applied just before the one-way traveltime surface t_1 of the direct wavefield. In our adapted scheme, the first truncation is applied at the two-way traveltime surface t_2 of a fictitious reflector in the subsurface, whereas the second truncation is applied by separating autocorrelated events from crosscorrelated events, using the traveltime surface t_0. We observe that t_0 can be picked naturally without relying on a macro model, by following the strong event that occurs at the origin of crosscorrelated data and adding some $\epsilon > 0$ to account for the bandlimited source signature. Because the second truncation is applied at one-way traveltime t_1 in the original Marchenko scheme, the moveout of this truncation depends directly on the macro model, rather than on the observed data. Hence, we can speak of our new truncation strategy as being data driven, versus the model-driven truncations that were prescribed by Wapenaar et al. (2014b). Potential advantages or disadvantages of both procedures may deserve further research.

CONCLUSIONS

We have derived a Marchenko equation that does not depend on a macro velocity model. To solve this equation, we require a two-way traveltime surface of a horizon in the subsurface and single-sided reflection data. Our solution is a data set, in which all interactions with the part of the medium above the selected horizon have been eliminated. The solution can be written as a series. By truncating this series, we can derive an algorithm for IME, which can be implemented by adaptive subtraction. If we apply the truncations just before the output time, rather than at the traveltime of a selected horizon, the prescribed procedure becomes similar to other IME schemes that have been derived from ISS. Similarities can also be found with particular data-driven IME schemes that predict all multiples, which have crossed a predefined horizon in the subsurface. However, unlike these specific schemes, internal multiples that have never crossed the specified horizon are also eliminated by the methodology that is proposed in this paper. Hence, the method can be applied at any horizon in the subsurface, without having to evaluate shallower horizons. The procedure has been demonstrated successfully on synthetic data, in which limitations exist due to diffraction-like discontinuities in the medium, fine layers, and a finite-acquisition

aperture. Because the method requires no macro model, it can be applied early in a seismic processing workflow, for instance, to improve velocity analysis, as we have demonstrated with semblance plots. In a field data test, the predicted internal multiples appeared to be kinematically correct, but we faced difficulties in subtracting these predictions from the input gathers.

ACKNOWLEDGMENTS

This research is financially supported by the Dutch Technology Foundation STW, applied science division of NWO, and the technology program of the Ministry of Economic Affairs (grant VENI.13078). A. Bakulin and P. Golikov (Saudi Aramco) are acknowledged for providing synthetic data. We thank J. Schuster, A. Abtheyab, X. Wang, B. Guo, G. Dutta (King Abdullah University of Science and Technology), J. Thorbecke, E. Slob, C. Reinicke, M. Staring, L. Zhang, J. Brackenhoff (Delft University of Technology), M. Ravasi, S. de Ridder, G. Meles, A. Curtis, C. A. da Costa Filho, K. Löer (University of Edinburgh), M. Dukalski, K. de Vos (Shell E&P), and J. Shragge (University of Western Australia) for their collaboration and for fruitful discussions.

REFERENCES

Abtheyab, A., X. Wang, and G. T. Schuster, 2013, Time-domain incomplete Gauss-Newton full-waveform inversion of Gulf of Mexico data: 83rd Annual International Meeting, SEG, Expanded Abstracts, 5175–5179.

Alá'i, R., and D. J. Verschuur, 2006, Case study of surface-related and internal multiple elimination on land data: 76th Annual International Meeting, SEG, Expanded Abstracts, 2727–2731.

Behura, J., K. Wapenaar, and R. Snieder, 2014, Autofocus imaging: Image reconstruction based on inverse scattering theory: Geophysics, **79**, no. 3, A19–A26, doi: 10.1190/geo2013-0398.1.

Berkhout, A. J., and D. J. Verschuur, 2005, Removal of internal multiples with the common focus-point (CFP) approach. Part 1: Explanation of the theory: Geophysics, **70**, no. 3, V45–V60, doi: 10.1190/1.1925753.

Berryhill, J. R., 1984, Wave-equation datuming before stack: Geophysics, **49**, 2064–2066, doi: 10.1190/1.1441620.

Broggini, F., R. Snieder, and K. Wapenaar, 2014, Data-driven wave field focusing and imaging with multidimensional deconvolution: Numerical examples from reflection data with internal multiples: Geophysics, **79**, no. 3, WA107–WA115, doi: 10.1190/geo2013-0307.1.

Cypriano, L., F. Marpeau, R. Brasil, G. Welter, H. Prigent, H. Douma, M. Velasques, J. Boechat, P. de Carvalho, C. Guerra, C. Theoro, A. Martini, and J. Nunes Cruz, 2015, The impact of inter-bed multiple attenuation on the imaging of pre-salt targets in the Santos basin off-shore Brazil: 77th Annual International Conference and Exhibition, EAGE, Extended Abstracts, N114.

da Costa Filho, C., M. Ravasi, and A. Curtis, 2015, Elastic P- and S-wave autofocus imaging with primaries and internal multiples: Geophysics, **80**, no. 5, S187–S202, doi: 10.1190/geo2014-0512.1.

da Costa Filho, C., M. Ravasi, A. Curtis, and G. Meles, 2014, Elastodynamic Green's function retrieval through single-sided Marchenko inverse scattering: Physical Review E, **90**, 063201, doi: 10.1103/PhysRevE.90.063201.

de Melo, F. X., M. Idris, Z. J. Wu, and C. Kostov, 2014, Cascaded internal multiple attenuation with inverse scattering series: 84th Annual International Meeting, SEG, Expanded Abstracts, 4113–4117.

El-Emam, A., K. S. Al-Deen, A. Zarkhidze, and A. Walz, 2011, Advances in interbed multiples prediction and attenuation: Case study from onshore Kuwait: 81st Annual International Meeting, SEG, Expanded Abstracts, 3546–3550.

Fokkema, J. T., and P. M. van den Berg, 1993, Seismic applications of acoustic reciprocity: Elsevier Science Pub. Co.

Fomel, S., 2006, Adaptive multiple subtraction using regularized nonstationary regression: Geophysics, **74**, no. 1, V25–V33, doi: 10.1190/1.3043447.

Griffiths, M., J. Hembd, and H. Prigent, 2011, Applications of interbed multiple attenuation: The Leading Edge, **30**, 906–912, doi: 10.1190/1.3626498.

Hadidi, M. T., and D. J. Verschuur, 1997, Removal of internal multiples: Field data examples: 59th Annual International Conference and Exhibition, EAGE, Extended Abstracts, A013.

Ikelle, L. T., 2006, A construct of internal multiples from surface data only: The concept of virtual seismic events: Geophysical Journal International, **164**, 383–393, doi: 10.1111/j.1365-246X.2006.02857.x.

Jakubowicz, H., 1998, Wave equation prediction and removal of interbed multiples: 68th Annual International Conference and Exhibition, EAGE, Extended Abstracts, 1527–1530.

Kelamis, P. G., W. Zhu, K. O. Rufaii, and Y. Luo, 2006, Land multiple attenuation: The future is bright: 76th Annual International Meeting, SEG, Expanded Abstracts, 2699–2703.

King, S., R. Dyer, and P. O'Neill, 2013, Data-driven internal multiple attenuation: Theory and examples: 83rd Annual International Meeting, SEG, Expanded Abstracts, 4096–4093, doi: 10.1190/segam2012-1298.1.

Liu, Y., J. van der Neut, B. Arntsen, and K. Wapenaar, 2016, Combination of surface and borehole seismic data for robust target-oriented imaging: Geophysical Journal International, **205**, 758–775.

Löer, K., A. Curtis, and G. A. Meles, 2016, Relating source-receiver interferometry to an inverse-scattering series to derive a new method to estimate internal multiples: Geophysics, **81**, no. 3, Q27–Q40, doi: 10.1190/geo2015-0330.1.

Luo, Y., P. G. Kelamis, S. Huo, G. Sindi, S. Hsu, and A. B. Weglein, 2011, Elimination of land internal multiples based on the inverse scattering series: The Leading Edge, **30**, 884–889, doi: 10.1190/1.3626496.

Malcolm, A. E., and M. V. de Hoop, 2004, A method for inverse scattering based on the generalized Bremmer coupling series: Inverse Problems, **21**, 1137–1167, doi: 10.1088/0266-5611/21/3/021.

Malcolm, A. E., M. V. de Hoop, and H. Calandra, 2007, Identification of image artifacts from internal multiples: Geophysics, **72**, no. 2, SI23–SI32, doi: 10.1190/1.2434780.

Matson, K., D. Corrigan, A. Weglein, C. Young, and P. Carvalho, 1999, Inverse scattering internal multiple attenuation: Results from complex synthetic and field data examples: 89th Annual International Meeting, SEG, Expanded Abstracts, 1060–1063.

Meles, G., K. Löer, M. Ravais, A. Curtis, and C. A. da Costa Filho, 2015, Internal multiple prediction and removal using Marchenko autofocusing and seismic interferometry: Geophysics, **80**, no. 1, A7–A11, doi: 10.1190/geo2014-0408.1.

Meles, G. A., K. Wapenaar, and A. Curtis, 2016, Reconstructing the primary reflections in seismic data by Marchenko redatuming and convolutional interferometry: Geophysics, **81**, no. 2, Q15–Q26, doi: 10.1190/geo2015-0377.1.

Ramírez, A. C., and A. B. Weglein, 2005, An inverse scattering internal multiple elimination method: Beyond attenuation, a new algorithm and initial tests: 75th Annual International Meeting, SEG, Expanded Abstracts, 2115–2118.

Ravasi, M., I. Vasconcelos, A. Kritski, A. Curtis, C. da Costa Filho, and G. A. Meles, 2016, Target-oriented Marchenko imaging of a North Sea field: Geophysical Journal International, **205**, 99–104, doi: 10.1093/gji/ggv528.

Schuster, G. T., 2009, Seismic interferometry: Cambridge University Press.

Singh, S., R. Snieder, J. Behura, J. van der Neut, K. Wapenaar, and E. Slob, 2015, Marchenko imaging: Imaging with primaries, internal multiples, and free-surface multiples: Geophysics, **80**, no. 5, S165–S174, doi: 10.1190/geo2014-0494.1.

Slob, E., K. Wapenaar, F. Broggini, and R. Snieder, 2014, Seismic reflector imaging using internal multiples with Marchenko-type equations: Geophysics, **79**, no. 2, S63–S76, doi: 10.1190/geo2013-0095.1.

Song, J., E. Verschuur, and X. Chen, 2013, Comparing three feedback internal multiple elimination methods: Journal of Applied Geophysics, **95**, 66–76, doi: 10.1016/j.jappgeo.2013.05.010.

Ten Kroode, P. E., 2002, Prediction of internal multiples: Wave Motion, **35**, 315–338, doi: 10.1016/S0165-2125(01)00109-3.

Van Borselen, R. G., 2002, Fast-track, data-driven interbed multiple removal: A North Sea data example: 64th Annual International Conference and Exhibition, EAGE, Extended Abstracts, F40.

Van der Neut, J., E. Slob, K. Wapenaar, J. Thorbecke, R. Snieder, and F. Broggini, 2013, Interferometric redatuming of autofocused primaries and internal multiples: 83rd Annual International Meeting, SEG, Expanded Abstracts, 4589–4594.

Van der Neut, J., I. Vasconcelos, and K. Wapenaar, 2015a, On Green's function retrieval by iterative substitution of the coupled Marchenko equations: Geophysical Journal International, **203**, 792–813, doi: 10.1093/gji/ggv330.

Van der Neut, J., K. Wapenaar, E. Slob, and I. Vasconcelos, 2015b, An illustration of adaptive Marchenko imaging: The Leading Edge, **34**, 818–822, doi: 10.1190/tle34070818.1.

Vasconcelos, I., K. Wapenaar, J. van der Neut, C. Thomson, and M. Ravasi, 2015, Using inverse transmission matrices for Marchenko redatuming in highly complex media: 85th Annual International Meeting, SEG, Expanded Abstracts, 5081–5086.

Verschuur, D. J., 1991, Surface-related multiple elimination: An inversion approach: Ph.D. thesis, Delft University of Technology.

Verschuur, D. J., 2013, Seismic multiple removal techniques: Past, present and future: EAGE Publications BV.

Verschuur, D. J., and A. J. Berkhout, 2005, Removal of internal multiple with the common focus-point CFP approach. Part 2: Application strategies and data examples: Geophysics, **70**, no. 3, V61–V72, doi: 10.1190/1.1925754.

Wapenaar, K., and E. Slob, 2014, On the Marchenko equation for multicomponent single sided reflection data: Geophysical Journal International, **199**, 1367–1371, doi: 10.1093/gji/ggu313.

Wapenaar, K., J. Thorbecke, J. van der Neut, F. Broggini, E. Slob, and R. Snieder, 2014a, Green's function retrieval from reflection data, in absence of a receiver at the virtual source position: Journal of the Acoustical Society of America, **135**, 2847–2861, doi: 10.1121/1.4869083.

Wapenaar, K., J. Thorbecke, J. van der Neut, F. Broggini, E. Slob, and R. Snieder, 2014b, Marchenko imaging: Geophysics, **79**, no. 3, WA39–WA57, doi: 10.1190/geo2013-0302.1.

Wapenaar, K., J. Thorbecke, J. van der Neut, E. Slob, F. Broggini, J. Behura, and R. Snieder, 2012, Integrated migration and internal multiple elimination: 82nd Annual International Meeting, SEG, Expanded Abstracts, doi: 10.1190/segam2012-1298.1.

Wapenaar, K., J. van der Neut, E. Ruigrok, D. Draganov, J. Hunziker, E. Slob, J. Thorbecke, and R. Snieder, 2011, Seismic interferometry by crosscorrelation and by multidimensional deconvolution: A systematic comparison: Geophysical Journal International, **185**, 1335–1364, doi: 10.1111/j.1365-246X.2011.05007.x.

Weglein, A. B., F. A. Gasparotto, P. M. Carvalho, and R. H. Stolt, 1997, An inverse scattering series method for attenuating multiples in seismic reflection data: Geophysics, **62**, 1975–1989, doi: 10.1190/1.1444298.

Ypma, F. H. C., and D. J. Verschuur, 2013, Estimating primaries by sparse inversion: A generalized approach: Geophysical Prospecting, **61**, 94–108, doi: 10.1111/j.1365-2478.2012.01095.x.